TECHNICAL REPORT

SPACE TELESCOPE SCIENCE INSTITUTE
Operated for NASA by AURA

Title: The JWST Point Spread Function: Calculation Methods and Expected Properties	Doc #: JWST-STScI-001157, SM-12 Date: 2 June 2007 Rev: -
Authors: R. B. Makidon, S. Casertano, C. Cox & R. van der Marel Phone: *410-338-4946*	Release Date: 8 June 2007

1.0 Abstract

We present a discussion of the methods that can be used to model the JWST Point Spread Function (PSF) and illustrate some of the potential impacts of the PSF properties on the scientific performance of the telescope. We summarize the quantitative PSF measurements typically used in astronomical imaging and evaluate those quantities on model NIRCam PSFs. These PSFs are generated using optical path difference (OPD) maps based on the most recent ("Revision T") JWST optical error budget. We discuss the dependence of the PSF on wavelength and compare the expected NIRCam PSF with PSFs from the HST/ACS, HST/NICMOS, and Spitzer/IRAC instruments. While high PSF quality in the near-IR is directly constrained by JWST requirements, we find that even at shorter wavelengths (e.g., 0.7 μm) the expected JWST PSF quality compares well with existing facilities. We evaluate PSFs for 10 different realizations of the error budget and show that PSFs with a wide range of properties are consistent with the present JWST design requirements. To allow evaluation of PSF properties under more general circumstances we also present a simple method to approximate the change in the OPD map and the resulting PSF induced by specific changes in the position of optical elements in the telescope+instrument system.

2.0 Introduction

Previous experience with other space telescopes, and in particular the Hubble Space Telescope (HST), has shown that the ability to obtain groundbreaking discoveries relies heavily on the quality and understanding of the telescope's point spread function (PSF). The critical elements are: (a) that the PSF is of the highest possible quality; (b) that the PSF is as stable as possible; and (c) that the PSF can be accurately modeled and understood during the data analysis stage. HST has a stiff monolithic temperature-controlled primary mirror. Changes in the HST PSF therefore arise almost exclusively due to variations in the distance of the secondary mirror from the primary mirror. These

changes occur at a level of microns both on an orbital timescale ("breathing") due to thermal variations associated with day-night transitions, and on a timescale of years due to desorption. The PSFs observed with HST therefore form essentially a one-parameter family. While other systematic PSF variations have been observed with HST (Makidon et al. 2006) these are so small that they don't affect HST science and weren't even discovered until 16 years after launch.

The situation will be quite different for JWST. The 6.5 m primary mirror consists of 18 semi-rigid segments. Each segment has 7 controllable degrees of freedom (tip, tilt, clocking, piston, two translations, and radius of curvature) and the secondary mirror has an additional 6 degrees of freedom (its radius of curvature cannot be varied). The telescope is passively cooled, but due to the changing attitude of the telescope with time (as it observes targets at different positions on the sky) the telescope will never be fully in thermal equilibrium. Thermal variations combined with the existence of 132 degrees of freedom will cause the parameter space of JWST PSFs to be much higher-dimensional than it is for HST. A wavefront sensing and control (WFS&C) system will enable the determination and subsequent correction of misalignments in the primary mirror segments and secondary mirror. This will ensure that the PSF never exceeds its total RMS wavefront error (WFE) requirement in the unvignetted Optical Telescope Element (OTE) field of view (FOV) of 131 nm RMS. However, as we show in Section 7.0 below, many different PSFs are consistent with the JWST WFE budget. Mirror updates will not occur more frequently than once every fourteen days. There is therefore considerable potential for thermal variations between mirror updates. This can cause important PSF variability, even if the PSF stays within its WFE budget at all times. Understanding slight variations in the properties of the PSF over both short and long timescales will be critical to achieving the goals of many science activities currently envisioned with JWST.

Another point of concern is the distribution of wavefront errors JWST will experience. In general, the errors that cause an optical surface to deviate from nominal can be divided into three regimes: low-, mid-, and high-spatial-frequency errors. Low-spatial-frequency errors, which can typically be characterized by Zernike polynomials, cause distortion in the system's wavefront that resemble classical aberration patterns (e.g, coma, astigmatism, defocus, and spherical aberration). These types of WFEs will be mitigated by JWST's WFS&C system. Mid-spatial-frequency errors cause small-angle scattering of light around the PSF centroid, reducing image contrast. High-spatial-frequency errors scatter light over larger angles, reducing total throughput in an optical system. Each WFE regime affects the science potential of JWST in different ways.

A good, stable PSF is critically important for many types of science envisioned with JWST. Requirements on image quality do exist to support his need, notably:

- **OBS-1607** (MR-110) Over the FOV of the NIRCam, the Observatory shall be diffraction limited at 2 μm defined as having a Strehl Ratio greater than or equal to 0.8.

- **OBS-88** (MR-113) Without requiring ground commanded correction, there shall be less than 2.0% root-mean squared (RMS) variation about the mean encircled

energy, defined to be at 0.08 arcsecond radius at a wavelength of 2 μm, over a 24-hour period.

- **OBS-90** (MR-115) The encircled energy within a radius of 0.08 arcsecond at 2 μm shall not change by more than 2.5% in less than 14 days following a worst case slew from a thermal equilibrium condition at the coldest pointing environment to the hottest pointing environment.

- **OBS-1599** (MR-228) The OTE unvignetted FOV shall have a WFE that is less than 131 nm RMS, within the dotted line boundary as shown in Figure 3-5 of the Mission Requirements Document (JWST-RQMT-000634 rev N, see Figure 1).

- **MR-384** The JWST System shall perform image-based wavefront sensing and control to meet all image quality requirements.

We note that there is no longer a requirement detailing the PSF anisotropy.

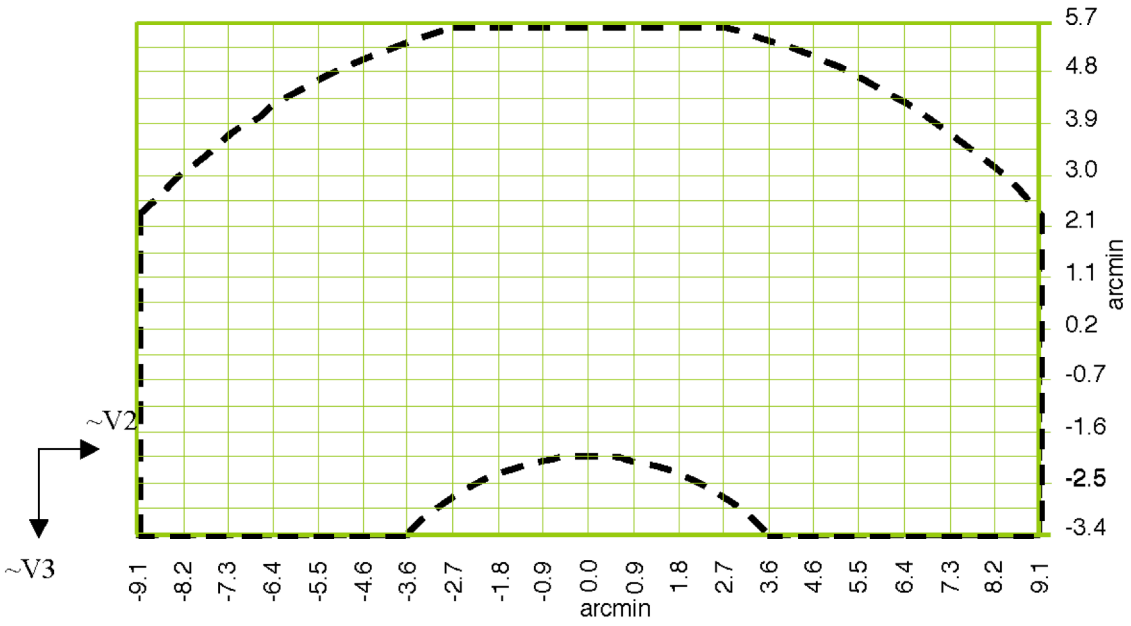

Figure 1: JWST Unvignetted Field of View, as defined in Figure 3-5 of the Mission Requirements Document (JWST-RQMT-000634 N). The dashed line boundary shown corresponds to an RMS wavefront error limit of 131 nm.

Will JWST meet the requirements as defined above? Recent work by Ball Aerospace has shown that the WFS&C Algorithms for Commissioning and Normal Operations appear to work in the laboratory environment of the 1 m Testbed Telescope (TBT). Extrapolation of these results to the 6.5 m JWST system (after accounting for the reduced noise floor) suggests the Algorithms should perform as well or better on orbit (Dean et al. 2007). A number of additional validation tests of the WFS&C Algorithms are planned, both via

observation using the TBT and by analysis using Ball Aerospace's Integrated Telescope Model.

A parallel analysis effort combining the work of individuals at Ball, Northrop-Grumman, ATK, and NASA's Goddard Space Flight Center has focused on the terms of the Wavefront Error Budget that represent predicted temporal instabilities in the JWST system. This effort, dubbed SDR4, is based on structural-thermal-optical performance (STOP) analysis of the deployed JWST Observatory (Bronowicki 2007). Wavefront error terms were grouped into optical path difference (OPD) errors and image motion errors. Image motion was converted to an equivalent wavefront error (WFE), and combined with OPD error to give the final stability result. What the SDR4 effort determined was that the encircled energy (EE) stability following an Observatory maneuver with the worst case combination of telescope dimensional stability and boresight alignment drift easily met the 24 hour requirement specified by OBS-88, but did not meet the 14 day required values specified by OBS-90. In particular, the SDR4 report noted that the change in EE within the first 24 hours of such a maneuver would be well below the 2% allowance, but the longer term stability would violate the 2.5% change requirement by Day 10, and could be as high as 4% by Day 14. When the WFE was decomposed into the first 22 Zernike polynomials, the largest impact on EE was found to be due to changes in the PSF arising from variations in the focus, 2nd and 3rd order 0-degree astigmatism, and 2nd order spherical terms. Clearly, improvements in this predicted behavior will be sought as the JWST hardware matures towards Flight.

While these and other modeling efforts are important contributions to the pre-Flight analysis of JWST's capabilities, in the end STScI will need to determine how best to operate the Observatory, balancing operational concerns while at the same time maximizing its science potential. Indeed, many science programs currently envisioned with JWST will depend on PSF properties beyond those captured by the requirements listed above. Some examples include:

- Planet transits: accurate measurements in all JWST instruments will rely on differential measurements acquired over timescales of hours; both photometric and spectro-photometric techniques will require an accuracy better than 0.1% over these timescales, necessitating an understanding of the PSF properties and centroids at the sub-pixel level.

- Planet detection (including coronagraphy): mid- and high-spatial frequency errors associated with JWST's optics will create a low-level scattered light 'halo' outside the PSF core and at large radii, reducing image contrast and system throughput. Experience with HST coronagraphy has shown that mid-spatial-frequency WFE in the HST optics coupled with thermally-induced focus variations has proven to be the limiting factor for high dynamic range imaging. While JWST will utilize a system to control much of the low-spatial-frequency WFE, mid-spatial-frequency WFE will remain unconstrained.

- Gravitational lensing studies: anisotropies of the PSF are an important contributor of systematic effects in measurements of gravitational lensing phenomena, especially in the very weak lensing regime leading to measurements of cosmic

shear and of large dark matter structures. HST has obtained several novel results via gravitational lensing, and JWST promises to enable significant progress, as long as the shape of its PSF, which directly affects the measurement of galaxy shapes, can be properly calibrated.

- Host galaxies of AGN: a high fidelity model of the PSF is needed in order to measure accurately the properties of host galaxies of distant QSOs and Active Galactic Nulcei (AGN). HST has demonstrated that, up to redshift $z \sim 2$, the properties of QSOs are closely related to those of their host galaxies. JWST will extend such studies to higher redshift, and – thanks to its sensitivity to the thermal infrared – will also be able to study the highly embedded (Type 2) AGNs which are invisible in the optical. As demonstrated by the HST experience, the ability to separate the light of the host galaxy from the central source very close to the center depends critically on the availability of a high fidelity model of the PSF.

- High precision photometry in crowded fields: HST has clearly demonstrated the advantage of high resolution *and stability* in the study of highly crowded stellar fields, such as near the cores of globular clusters and in nearby galaxies. High photometric accuracy is critical to resolving the star formation history of such systems. The study of Cepheid variables and the determination of H_0 is also critically dependent on stable, reliable photometry in crowded fields. Variations in the PSF, especially in its core, inevitably cause photometric uncertainties, in particular for PSF fitting procedures – which are most useful in very crowded fields. Therefore understanding and constraining variations in the core of the PSF is key to predicting the crowded-field photometric performance of JWST.

While a massive integrated modeling effort along the lines of SDR4 could help provide an understanding of the JWST PSF response to thermally-induced variations for a limited number of cases, such an effort is far too cumbersome to support on-orbit analyses. Clearly, STScI will need some means to model the behavior of the PSF in response to small movements of optical elements. In addition, scientists observing with JWST will need relatively simple and robust tools that will enable them to model and ultimately understand the JWST PSF for a variety of observing situations and approaches, similar to the tools that exist to support HST observations. Currently, most JWST optical models are only available as CODE V macros, software that is impractical for use by the average astronomer.

Therefore, we summarize here some first results from our analysis of a variety of simple approaches to model the JWST PSF. We focus our attention on the comparison of a number of quantities of interest to astronomical investigations, including the Encircled Energy, the Full Width at Half Maximum (FWHM), and the sharpness. We also discuss the main PSF properties that will be common to all JWST science, to provide users a basic understanding of what they'll have to deal with. We examine the differences between the various PSF modeling approaches, in an attempt to determine which quantities can be reliably estimated using simple models, and which quantities require more sophisticated modeling to achieve sensible results.

3.0 Available Modeling Approaches

There are numerous approaches to optical modeling that are available to the scientific and engineering community. However, with a few exceptions, many of the tools used in the analysis of optical systems can be grouped into one of three broad categories: those that primarily utilize ray tracing; those that primarily manipulate wavefronts, including plane-to-plane propagators; and hybrid routines that utilize both ray tracing and wavefront manipulation. Each approach has its own strengths and weaknesses, depending on the task at hand.

What follows is a discussion of specific optical modeling tools available to the JWST Project. We start with the tools we are most familiar with (including one written in-house), and work toward the tools that we have either not invested resources in or are not available to us directly. This list is not intended to be a complete list of optical modeling tools used through the Project; rather, it is a synopsis of the tools the authors have become familiar with over the last few years.

3.1 Point Spread Modeling using JWPSF

JWPSF (Cox and Hodge 2006) was initially written by C. Cox and P. Hodge in the summer of 2005 as a user-friendly means to model the PSF at representative locations in the JWST optical train (including the respective instrument focal planes) at a variety of wavelengths. JWPSF was written in the Python programming language, and makes use of freely available compilers and software for analysis and visualization. JWPSF has continued development since its initial release, with version 2.0 released in the fall of 2006.

3.1.1 Computation

At its core, JWPSF is a wavefront manipulation tool that assumes the Fraunhofer approximation to the Fresnel-Kirchhoff diffraction integral is valid, thus allowing the complex electric field in the image plane to be represented by the Fourier transform of the phasor of the wave front phase in the pupil plane (see Section 5.1). JWPSF only requires a binary pupil image (generally, a FITS file describing the aperture, with regions of perfect transmission and occultation valued at 1.0 and 0.0 respectively) to generate a PSF. Aberrations can be incorporated via optical path difference (OPD) files[1], which describe the difference in phase between an ideal wavefront and the wavefront produced by the optical system as displacements at each point on the wavefront. Since JWPSF can be used to model PSFs at a variety of wavelengths, OPD displacements used by JWPSF are provided in physical units (e.g., nanometers).

[1] The OPD files available with the JWPSF releases have been supplied by Ball Aerospace, and are based on their modeling of the JWST error budget for the planned Science Instruments. Initial OPDs were based on the Rev R error budgets, though OPDs based on the Rev T error budget have recently become available, and are used exclusively in the analyses presented in this report. We should note that JWPSF will accept OPDs from any source, as long as the OPDs are in physical units.

The wavefront phase $\phi(x,y)$ over the aperture depends on the wavelength λ being modeled, and is simply the OPD at each point (x,y) multiplied by 2π/λ. JWPSF determines the phase from the OPD, calculates the phasor $e^{i\phi(x,y)}$[2], and multiplies the phasor by the pupil image to form the complex aperture illumination function $A_\phi(x,y) = A(x,y)e^{i\phi(x,y)}$. The Fraunhofer diffraction amplitude at the image plane is given by the Fourier transform of $A_\phi(x,y)$,

$$\psi(u,v) = FT\left\{A_\phi(x,y)\right\},$$

and the corresponding PSF given by the modulus square of $\psi(u,v)$,

$$I(u,v) = \left|\psi(u,v)\right|^2.$$

The PSF resulting from the above calculation is given in units of λ/D, where D is the diameter of the aperture. To interpret these calculations in physical terms (e.g., NIRCam detector pixels), we need to specify the pixel scale and image size of the initial pupil and phase images. We typically start with an oversampled PSF, which we produce by embedding our aperture array within another zero-filled array that is larger than the actual aperture diameter by a factor F (the only limitations to the choice of F are available computer memory and processor time). The resultant angular scale of the pixels in the PSF image is then given by $\lambda/(F \cdot D)$. As an example, if our 6.5m JWST aperture spans D = 512 pixels in diameter, and we assume F = 4, our input aperture array will span 2048 pixels on a side, and our resultant pixels would each span an angle of $\lambda/4D$ radians. At a wavelength λ =1μm, this corresponds to 3.84 x 10^{-8} radians or 7.9 milli-arcseconds per pixel. As an aside, we note that with D = 512 pixels over a 6.5m diameter, each pixel in the aperture plane spans 12.69 mm, thus limiting the spatial Nyquist length of structures we can accurately describe in the pupil to twice this value (25.39 mm).

[2] The phasor $e^{i\phi(x,y)}$ represents the electric field corresponding to the phase $\phi(x,y)$.

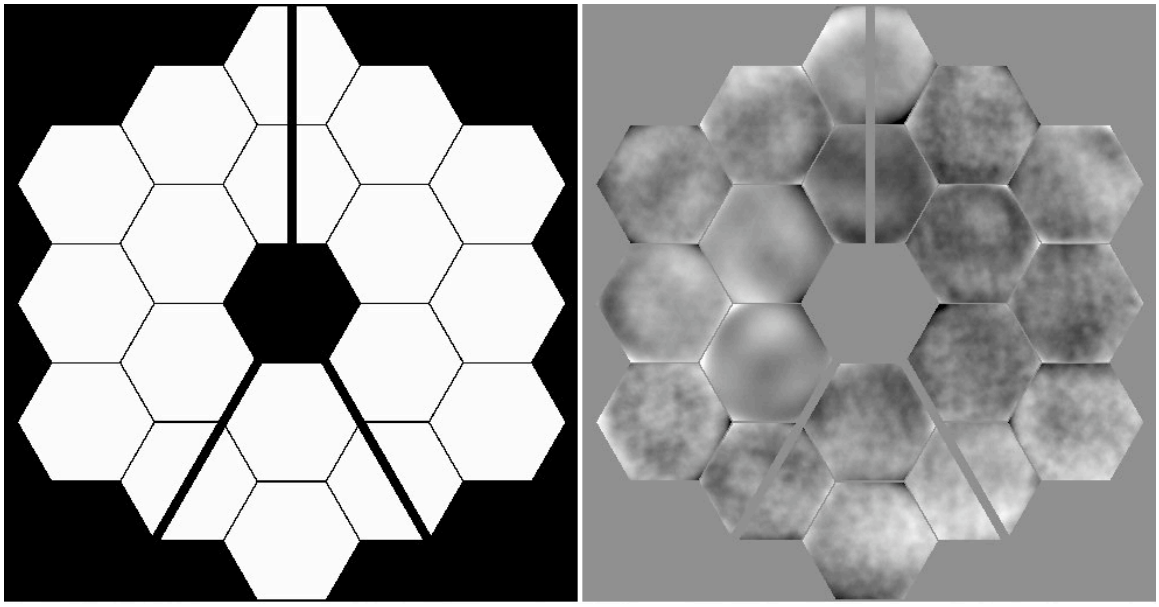

Figure 2: Illustration of the pupil image and Optical Path Difference files, being the amplitude and phase of the complex pupil image supplied to the software. The eighteen hexagonal mirrors are shown and the three secondary mirror supports. In the pupil image zero is represented by black, while in the OPD image zero is mid-grey.

3.1.2 Multi-wavelength Simulations

While the calculation described above was specified for a single wavelength λ, PSFs spanning multiple wavelengths (e.g, over a specified NIRCam bandpass) can be calculated by assuming a broadband PSF is just a weighted sum of individual monochromatic PSFs within that bandpass. The weights applied to each wavelength's PSF can be calculated as a product of a source spectrum (in the case of a simulated astronomical target) and a filter throughput at that wavelength.

For JWPSF, source spectra are extracted from the Kurucz models supplied in the HST library. The particular spectra are selected by stellar type. A subset of these spectra is supplied as part of the program package. Source spectra are given in units of ergs cm^{-2} s^{-1} A^{-1}. For use in the PSF modeling we need photons/sec and so the spectra are multiplied by the wavelength currently being simulated. The absolute flux is not considered for the generation of PSF shapes; each image is self-normalized to give unity total flux.

Filter throughputs have been generated as top hat shapes based on nominal filters proposed for the JWST instruments. Other real or synthetic filter shapes may be used by supplying FITS tables of wavelength and throughput. Given a filter profile we divide it up into a number of equal width wavelength bands straddling the range for which the throughput is more than 1%. For each band we form the integrated product of filter throughput and spectral intensity to give a weighting factor for the wavelength at the center of each segment. The number of segments is user selectable. Each monochromatic PSF to be included in the weighted sum (multi-wavelength) PSF is also scaled to physical pixel units before summation. Since the output pixel scale is a function of wavelength, a

reference pixel scale is chosen (e.g., based on the bandpass central wavelength), and resultant PSFs at other wavelengths are interpolated onto the reference pixel scale.

3.2 ZEMAX

ZEMAX[3] is commercially available optical system design software used primarily for lens design, illumination, stray light, and beam propagation studies. Unlike most commercial optics design software, ZEMAX is fairly inexpensive, and has a (relatively) shallow learning curve: one can be working with simple optical designs in a few minutes.

ZEMAX models optical systems using two basic modes: sequential and non-sequential ray tracing. In sequential mode, all ray propagation occurs via a linear or sequential path, e.g. rays propagate from the primary mirror to the secondary mirror through the focal plane. Sequential modeling has proven useful for relatively simple optical systems such as those used for the HST's imaging cameras. In non-sequential mode, there is no pre-defined sequence of surfaces for ray propagation. The surfaces (or objects) that interact with propagating rays are solely determined by the physical positions and properties of those objects along with the propagation direction of the rays of interest. Modeling how the rays from a point source interact with the individual JWST primary mirror segments would show the most benefit from non-sequential ray propagation.

At its core, ZEMAX is ray-tracing software with a powerful suite of optimization tools, as well as extensive tolerancing capabilities. While these capabilities are extremely important in the design of and the determination of the basic properties of optical systems (such as magnification, low-order aberrations, vignetting, etc.), they cannot predict the effects of diffraction. To study diffraction, one needs to model how the electromagnetic wave is diffracted as it propagates from one optical surface to another (e.g., physical optics propagation). Conversely, most software used for physical optics propagation cannot be used to calculate aberration changes caused by a shifted component in the optical train. To remedy this, recent versions of ZEMAX have added physical optics propagation capabilities, allowing users to model phenomena such as interference, holography and near/far field diffraction. However, we have no experience to validate the robustness or accuracy of physical optics propagation with ZEMAX.

ZEMAX's low cost and relative flexibility have made it popular with educational institutions. Significant expertise with ZEMAX already exists at the STScI, and a handful of simple JWST models exist in ZEMAX-readable formats. However, ZEMAX is not a standard tool for industries that rely on optical design software, which instead prefer tools such as CODE V[4]. Consequently, all JWST optical models are required to be delivered to the Project as CODE V macros, limiting the availability of ZEMAX models for most of JWST's critical components. However, some useful JWST models do exist in ZEMAX, as we describe below.

[3] ZEMAX is a trademark of the ZEMAX Development Corporation.
[4] Code V is a trademark of Optical Research Associates.

3.2.1 NIRCam with a Monolithic Primary Mirror

In December 2006, we received a set of ZEMAX prescriptions from M. Rieke that describe the NIRCam optical components for both the short-wavelength and long-wavelength modules. The models are only accurate for wavelengths of 2.0 μm and 3.5 μm respectively, a result of how cryogenic refractive indices are handled in ZEMAX.

For simplicity, the NIRCam modules are "fed" by rays from a monolithic JWST Primary Mirror. The Secondary Mirror, Tertiary Mirror, and Fine Steering Mirror are all modeled with simple (circular) geometries.

The models, as received, assumed an entrance aperture placed 5593.443 mm in front of the JWST Primary (along the +V1 axis), between the Primary and Secondary Mirrors. This location for the entrance aperture eliminated any obscuration of incoming rays from either the Secondary Mirror or its support structure. We have since amended this prescription to place the entrance aperture behind the Secondary Mirror, and now account for both the Secondary Mirror obscuration and a simplified model of the SM support structure (see Figure 3).

While the distances between OTE optical elements correspond to those specified in the "JWST OTE Optical Prescription" (JWST-SPEC-005394 Rev B), we have noticed that both the original and amended ZEMAX prescriptions for the OTE+NIRCam exhibit a slight defocus at the NIRCam image plane (0.0215 waves and 0.0202 waves RMS in the original and amended models respectively). The source of the defocus has not been determined.

Though ZEMAX has the ability to interact with other programs (e.g., MATLAB, Visual Basic, or C/C++) using a built-in Dynamic Data Exchange (DDE) server, we have not yet explored using this capability with software we are more familiar with (IDL[5] and Python). As a consequence, retrieving PSFs from the aforementioned ZEMAX models has required the export of an OPD map at the exit pupil to a text file and converting that text file to a FITS file for use with JWPSF. We will continue to explore more interactive means to use IDL and Python with ZEMAX as our modeling needs become more complex.

[5] The Interactive Data Language (IDL) is a trademark of Research Systems, Inc.

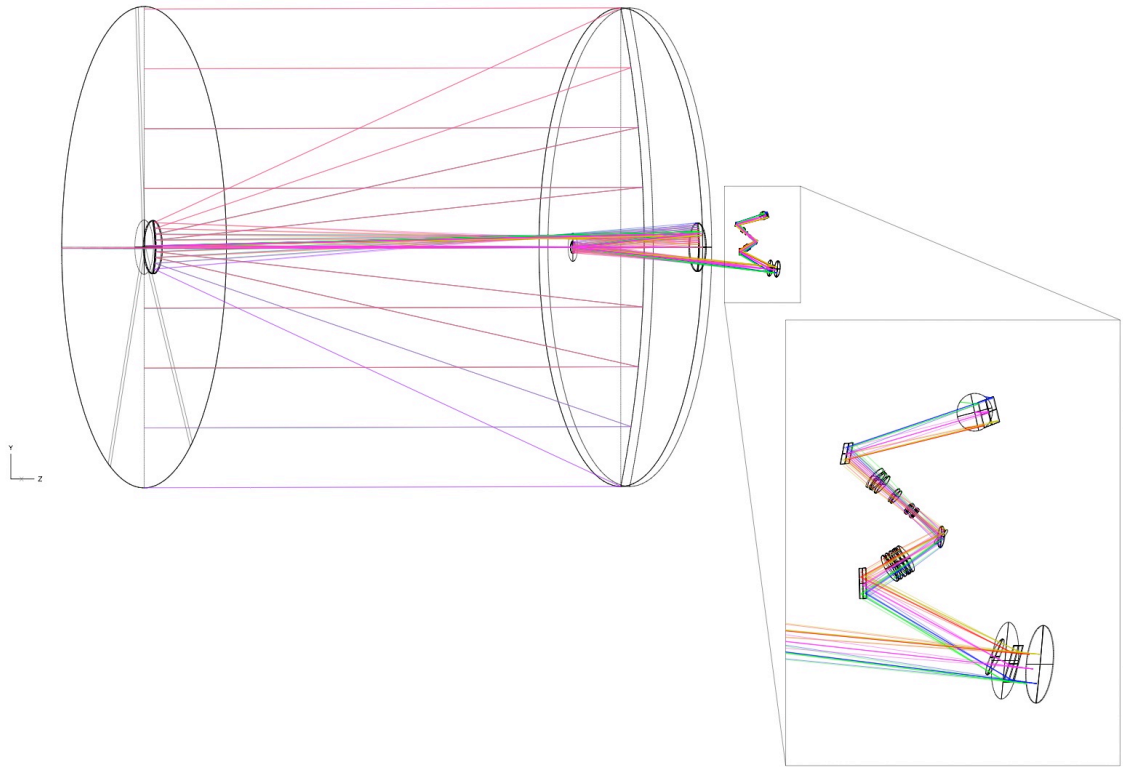

Figure 3: A sequential-mode ZEMAX ray trace model of a monolithic JWST primary mirror and the NIRCam short-wavelength module.

3.2.2 NIRCam with a Segmented Primary Mirror

While a simple, monolithic OTE model is useful to examine low-order properties of the JWST OTE and NIRCam (such as tilts or decenters of specific optical components), a more thorough understanding of JWST imaging will require modeling the segmented Primary Mirror and associated OTE optics. Modeling a segmented Primary Mirror in ZEMAX will require the move from a sequential model of the OTE to a non-sequential model, with each individual Primary Mirror Segment independently defined.

In February 2007, we received a ZEMAX non-sequential model of the segmented-Primary Ball Testbed Telescope (TBT) from Erin Sabatke at Ball Aerospace. While there are many parallels between the TBT and JWST, there are a number of differences that would make the conversion of the TBT model to a flight-like model challenging. Given time, we can build a segmented model for JWST in ZEMAX. However, CODE V macros with a segmented JWST OTE, flight instruments (including NIRCam), and WFS&C hardware components (weak lenses, DHS, PIL) already exist, both at Ball and with the Project. As such, producing a segmented primary ZEMAX model may not prove to be the best use of the resources available to the STScI.

3.3 PROPER

PROPER[6] is a library of optical propagation procedures and functions for the IDL environment, developed by John Krist at JPL to support the NASA Terrestrial Planet Finder Coronagraph project. Unlike ray tracing tools such as ZEMAX and CODE V, which calculate the path of individual rays through the components of an optical system, PROPER consists of a set of wavefront propagation tools that calculate the changes in the electromagnetic field as it travels through the optical system. PROPER was designed as a tool to explore the effects of diffraction in optical systems, and as such is not suited for detailed optical design work.

A significant advantage of PROPER is that its library function and procedure calls exist within the IDL environment. As such, PROPER calls may be interleaved with additional user-written code, taking advantage of the wide range of mathematical, array processing, file input/output, and graphical routines available in IDL, providing a versatile system for modeling. In addition, PROPER includes procedures to create apertures and obscurations (circular, elliptical, rectangular, polygonal, and hexagonal arrays) and apply aberrations (e.g., low-order Zernike polynomials, error maps defined by power-spectrum-density profiles, deformable mirrors, and user-defined wavefront error maps).

The PROPER routines have been designated as Technology and Software Publicly Available ("TSPA"), and are freely available from Open Channel Software (www.openchannelsoftware.com). PROPER is provided as IDL source code, enabling the user to modify or make changes to the routines as necessary.

Despite the advantages noted above, there are a few disadvantages to PROPER. Currently, all official JWST optical models are delivered to the Project as CODE V macro (.seq) files. At this time, there is no functionality within PROPER to automatically convert a CODE V macro to a PROPER prescription (though such functionality could conceivably be written by the user running PROPER). As such, PROPER models for the JWST OTE and accompanying instruments must be translated either from design documents or from the CODE V macros themselves.

At the time this document was written, PROPER was still considered beta-release software, and as such does still contain a few elements that need further testing. For example, the PROPER v0.9 release does not reliably model optical systems with three or more non-spherical components (such as the three-mirror anastigmat design for the JWST OTE). While some limited JWST functionality does already exist in PROPER, further development is required. Models of the JWST OTE are currently best represented by a single optic (the Primary Mirror) with a focal length of 131.4 m and an accompanying phase map consisting of random phase errors for each hexagonal segment plus global errors over the aperture.

[6] PROPER is © 2006, 2007 California Institute of Technology ("Caltech").
Check with the JWST SOCCER Database at: http://soccer.stsci.edu/DmsProdAgile/PLMServlet
To verify that this is the current version.

3.4 Other Optical Modeling Tools In Use by JWST Parties

In the previous subsections, we've listed optical modeling tools developed by or in use at STScI. What follows is a brief description of optical modeling tools in use by other parties to the JWST Project. This list is by no means comprehensive, but is included to help provide some context to other modeling efforts underway through the Project.

3.4.1 CODE V

CODE V is the industry-leading optical design software, used to model, analyze, optimize, and provide fabrication support for the development of optical systems with diverse applications. Like ZEMAX, CODE V provides a powerful, yet easy-to-use toolkit of optical techniques and calculations.

All models of JWST optical systems and components are required to be delivered to the Project as CODE V macros. A large number of models, including a segmented JWST OTE, flight instruments (including NIRCam), and WFS&C hardware components (weak lenses, DHS, PIL) are already available from the Project.

However, CODE V is expensive, and experience in using CODE V at STScI is very limited. Purchasing and maintaining a CODE V license for our use requires a significant commitment of both time and money.

3.4.2 OSLO

OSLO[7] – Optics Software for Layout and Optimization of optical systems – is a product of Lambda Research Corporation, and is used primarily to determine the optimum sizes and shapes of the elements in optical systems. OSLO can be used to simulate the performance of optical systems using both geometrical (ray tracing) and physical optics.

OSLO is seen by many as the "middle ground" between the ease of use presented by ZEMAX and the power provided by CODE V. Though not as prevalent through the JWST Project as CODE V, some OSLO models do currently exist for various JWST components.

Like CODE V, obtaining and maintaining a license for OSLO is expensive, and experience with OSLO here at STScI is limited.

3.4.3 MACOS

MACOS (Modeling and Analysis for Controlled Optical Systems) is a package developed at JPL by Dave Redding and collaborators dedicated to fast, accurate and detailed optical models. MACOS has a full diffraction propagation capabilities combined with ray trace and differential ray trace modeling.

MACOS has been used extensively with structural and thermal modeling tools such as NASTRAN and TRASYS/SINDA, primarily using MATLAB as a means to tie structural variations together with the optical models. More recently, MACOS has been incorporated into JPL's Integrated Modeling of Optical Systems (IMOS) package.

---

[7] OSLO® is a registered trademark of Lambda Research Corporation.

Many JWST models are defined in MACOS, a result of the early involvement of JPL in the JWST project and in WFS&C. Currently, MACOS provides the basis for an optical "model server" for use with TBT modeling. A flight-like JWST model server is reported to be under development.

3.4.4 MATLAB

MATLAB[8] is a high-level technical computing language and interactive environment for algorithm development, data visualization, data analysis, and numeric computation. MATLAB is used in a wide range of applications, including signal and image processing, communications, control design, test and measurement. Add-on toolboxes (collections of special-purpose MATLAB functions) extend the MATLAB environment to solve particular classes of problems in these application areas.

MATLAB provides a number of features that allow for the integration of MATLAB code with other languages and applications. It is in this mode that MATLAB has proven the most useful for optical modeling, tying together structural and thermal modeling efforts with ZEMAX, CODE V, and MACOS optical models. Ball Aerospace has reported developing optical models within the MATLAB environment itself for use with their proprietary test modeling software

3.4.5 ITM

The Integrated Telescope Model (ITM) is an integrated modeling environment for telescope performance modeling and analysis. Developed by Ball Aerospace, the primary use of ITM on the JWST project has been the testing, verification, and validation of the WFS&C analysis algorithms.

ITM was designed to seamlessly integrate models in structural dynamics, optics, controls, signal processing, detector physics, and disturbance modeling into one cohesive model to support efficient system level trades and analysis. The core of ITM is formed by the optical toolbox implemented in MATLAB, though interfaces with CODE V and OSLO models have also been implemented.

ITM is a performance-modeling tool, and is not a replacement for optical modeling tools such as CODE V or OSLO. ITM is Ball proprietary software, and its availability outside of Ball Aerospace is strictly limited.

3.4.6 ASAP

The Advanced Systems Analysis Program (ASAP[9]) is an industry standard in optical engineering software. Though not as prevalent as CODE V or ZEMAX for astronomical-related optical design, ASAP is used by industries to predicts the real-world performance of automotive lighting, bio-optics, coherent systems, displays, imaging systems, lightpipes, luminaires, and medical devices.

[8] MATLAB® is a registered trademark of The MathWorks, Inc.

[9] ASAP® is a registered trademark of Breault Research Organization

For the JWST project, ASAP has been used primarily to model surface (BRDF) and volume scattering for JWST components, including the Yardstick design for the sunshield and dust contamination off the NIRCam Pick-Off Mirror.

ASAP, though extremely powerful, appears to be well beyond the scope of the work we expect to do at STScI prior to and after the launch of the Observatory.

4.0 Quantitative measures of PSF properties

Traditionally, the quality of a PSF is measured by a number of simple metrics that identify and measure relevant characteristics. The *Strehl Ratio*, the ratio of the peak of the PSF in comparison to the peak of a comparison PSF corresponding to the same pupil area (including obstructions and gaps) but free from wavefront errors, is a very useful indication of how well the optical train performs, and is closely related to the quality of the PSF core. A related measure is the *Peak Pixel* value of the normalized PSF. This quantity is not a very robust measure for actual observations because it depends on the centering of the PSF relative to the pixel center. However, it can be useful for relative comparison of model PSFs that are all centered in exactly the same way. The *Full Width at Half Maximum* (FWHM) measures the size of the PSF core, and is especially relevant in comparison to ground-based observations. For space-based instruments, the FWHM is often measured not directly on the PSF itself, but rather on a best-fitting functional form – often a Gaussian. Since the actual PSF deviates significantly from the functional form used, the measured FWHM depends significantly on the region used for the fit. The *encircled energy* measures the fraction of the light enclosed within a given radius, and by extension the radius-dependent aperture correction used in aperture photometry. In particular, the energy encircled within a radius comparable to the first Airy ring measures the impact of medium-angle scattering, which is especially important to characterize coronagraphic performance. The encircled energy within a large radius (1" or larger) measures the *large-angle scattering* properties of the PSF, , which impacts the amount of diffuse light in regions with a high density of point sources.

In addition to these classic PSF metrics, we introduce a number of additional metrics which bear a direct quantitative relation to the performance of JWST for different science investigations. Such metrics include: *Image Sharpness*, which measures the number of noise pixels for optimal extraction (PSF fitting); *PSF cross-correlation*, which tracks the stability and residuals of PSF fitting procedures; and *PSF Anisotropy*, which relates to the PSF performance for shape measurements of compact objects (e.g., distant galaxies in weak lensing measurements). We discuss several of these metrics in the subsections below, and apply these measures to simulated monochromatic and multi-wavelength PSFs in the following sections.

4.1 Encircled energy

Encircled energy is defined as the fraction of total flux that falls within a specified radius. Different choices of radii are relevant for different purposes. The JWST requirements specify the encircled energy within a radius of 80 mas, which is especially relevant to

bound the medium-scale (sub-segment) irregularities of the JWST primary and relates closely with its coronagraphic performance.

Encircled energy is also directly related to the performance of aperture photometry, which is the most widely used form of photometry for HST images. Point-source fitting photometry can in principle achieve better signal-to-noise ratio and separation from nearby sources, but it is more complex, requires a very accurate, oversampled model of the PSF, and is very sensitive to changes in the PSF itself; for these reasons, many HST users prefer aperture photometry even for point sources in crowded fields. HST experience suggests that a good choice of radius for aperture photometry is between 1.5 and 2.5 pixels; larger radii accrue a significant penalty in signal-to-noise ratio and are not suited for moderately crowded fields. In the following we report the encircled energy within a number of radii: the first local minimum of the PSF profile, which is the broad-band equivalent of the first Airy ring; 50 mas, suitable for crowded-field photometry in NIRCam's short-wavelength camera; and 150 mas, probably a good choice for robust photometry of bright, isolated choices.

Especially important is the *temporal stability* of the encircled energy, which directly affects the photometric stability of the instrument. A change in the encircled energy with respect to its reference value causes a photometric error equal to that change as a fraction of the encircled fraction itself, not as a fraction of the total. For example, if the encircled energy changes from 50% to 49%, the photometric error is 2% (0.01/0.50), not 1%. Changes in encircled energy as a function of source location are to be expected, and are routinely calibrated on HST as position-dependent aperture corrections; changes due to variations in the PSF vs. time are not usually calibrated on HST, and – if significant on JWST – will require a more elaborate calibration program. Variations on short time scales may require self-calibration within each image, which depends on the availability of sufficiently bright and isolated sources and may not always be practical.

4.1.1 Large-angle scattering

Large-angle scattering (beyond ~ 1") affects the level of background that might be observed in the vicinity of very bright sources, or in a very crowded field. Since the details of the impact depend on the density and luminosity distribution of bright sources, we do not attempt to quantify the background increase due to large-angle scattering, but simply track the fraction of energy deposited beyond 1" as a relative measure of the degree to which different PSFs may be effective in crowded fields or near luminous sources.

4.2 Image sharpness

The image sharpness S is defined as the sum of the PSF P squared over all pixels:

$$S = \sum P^2$$

Note that the sum must be executed over the actual detector pixels, not on the oversampled PSF. For a well-sampled PSF, S varies little as function of the subpixel centering of the image.

The usefulness of the image sharpness is due to the fact that it is directly related to the signal to noise ratio that can be achieved for a faint point source. The reciprocal of the sharpness is the number of *effective noise pixels* to be used when estimating the background noise contribution. If a source is detected with C counts, and each pixel has B equivalent noise counts, then the total signal-to-noise ratio SNR of the detection is given by:

$$SNR = C/\sqrt{C + B/S}$$

In this expression, $1/S$ has the role of the number of pixels that contribute their noise to the detection. Note that the expression above is approximate; for example, it does not include the effect of uncertainties in the source position and in the background level determination, and it assumes that the fitting takes place over an arbitrarily large area in which the target is the only significant source. If the fitting is restricted to a small area A, the effective sharpness S_A to be used in the signal to noise expression is defined simply as:

$$S_A = \sum_A P^2 \Big/ \left(\sum_A P \right)^2$$

with the counts similarly restricted to those in the relevant area.

Despite its limitations, image sharpness is very useful in estimating the point-source sensitivity of different instruments and modes. However, sharpness should not generally be used to indicate image quality, as it is primarily a function of sampling; a well-sampled PSF always has a small sharpness (0.060 for a perfect Airy function with Nyquist sampling). The image sharpness can only be unity if *all* the flux falls into one pixel, which is unphysical and generally not a desirable goal. For NIRCam, the sharpness is expected to decrease with increasing wavelength even in the short channel, as the increasing wavelength spreads the PSF over a larger area – this despite the poorer image quality at shorter wavelengths.

4.3 PSF cross-correlation and residuals

An accurate, pixel-by-pixel model of the PSF is critical not only for PSF-fitting photometry, but also for science investigations that require the detection of faint targets very close to bright point sources. Examples include the separation of very close binaries, often with large magnitude differences, and the study of host galaxies of bright QSOs; in both cases, the faint source may be too close for coronagraphy, and fitting and subtraction of the bright source may be the only option. Such a model can be obtained empirically, from many, well-dithered observations of point sources with the correct color, or theoretically, from accurate models of the optics and detector properties of each instrument. The model also needs to be adjusted for the correct sub-pixel centering of the bright source, such as the effective PSF model of King and Anderson (2000). We assume that such knowledge is indeed available.

However, even if the PSF model is perfectly known at one time, variations in the PSF will lead in inaccuracies in the fitting procedure. For PSF-fitting photometry, such

variations lead to photometric errors that can be quantified by the PSF cross-correlation. For PSF subtraction, variations lead to residuals that limit the accuracy of the underlying investigation.

The photometry error can be easily estimated via the cross-correlation between the reference PSF P_1 (used in the fitting) and the actual PSF at the time of observation P_2; the cross-correlation ψ is defined as:

$$\psi = \sum P_1 P_2$$

which is strictly < 1 unless $P_1 = P_2$, and the photometry will be underestimated by the amount $1 - \psi$. When realistically restricted to an area A, the cross-correlation is defined as

$$\psi_A = \sum_A P_1 P_2 \Big/ \sum_A P_1^2$$

which can be > 1 if P_2 has a larger fraction of flux within area A than P_1.

Residuals from the PSF fitting procedure can lead to incorrect identification, e.g., of possible faint point sources near the bright source, or increase the sensitivity threshold for such sources. They can also affect the ability to separate the light of the central source from diffuse light around it, e.g., in a circumstellar disk or in a QSO host galaxy. The optimal metric for the PSF residuals will differ depending on the science project. For the detection of faint point sources, a good metric would be the largest residual after convolution with the PSF itself, which would indicate the flux of a spurious source identified in the subtraction residual. For detection of faint extended components, the effect of the residual light on the estimated properties of such components would be more relevant. The largest discrepancy is usually in the central pixel, and can exceed several tens of percent of its value; however, the central pixel is generally excluded from the science analysis of such images, as the light in that region is difficult to disentangle from the central point source. As a starting point, we report the peak absolute residual in pixels between 50 and 150 mas from the PSF center, which is the region where PSF subtraction is the most likely approach; beyond 150 mas, a coronagraphic approach may well be preferable.

4.4 Anisotropy measures and weak lensing

Weak lensing measurements are based on the apparent shape of galaxy images on the sky. In a typical weak lensing measurement, the shapes of thousands of galaxies are measured and averaged out, in order to remove the randomness of their intrinsic shape and determine the underlying systematic distortion due to the propagation through the gravity field of visible and dark matter lying along the line of sight. In the most demanding applications, measuring cosmic shear, the typical effect sought is of order of a few percent, and it needs to be measured with a relative accuracy of a part in ten, thus leading to a desired accuracy in the final measurement of about 0.1%. Individual measurements typically have much larger errors, which are reduced by averaging over

thousands of galaxies; however, any uncorrected systematic effects at the level of 0.1% will ultimately limit the accuracy of weak lensing measurements.

The optical/detector train introduces several distortions in each galaxy image. First, the images are broadened by convolution with the PSF, which effectively dilutes the effect of the lensing shear. Second, any asymmetry of the PSF results in an asymmetry of the detected image; such asymmetries are likely to be correlated for nearby galaxies, and therefore effectively mimic lensing shear. Third, the detected image is pixellated, which a) further softens the image by convolution with the pixel response function, and b) introduces aliasing unless the image is properly sampled. Fourth, the detection process introduces noise in the image, which limits the accuracy with which the shape of each galaxy image can be measured. All of these effects are important in practice; here we focus on the first two, which depend directly on the properties of the PSF and can be estimated, at least coarsely, from the PSF itself. It is important to realize that optical and detector effects act as systematic terms, in that they do not necessarily abate as more sources are observed; therefore they must be understood and calibrated at least to the level of accuracy in the shear measurement ultimately desired. The treatment below follows closely that in Casertano (2002).

The shape of the PSF can be measured from its weighted second-order moments:

$$P_{xx} = \sum (x - P_x)^2 Pw \Big/ \sum Pw$$

$$P_{xy} = \sum (x - P_x)(y - P_y) Pw \Big/ \sum Pw$$

$$P_{yy} = \sum (y - P_y)^2 Pw \Big/ \sum Pw$$

where P_x, P_y are the similarly defined first-order moments and w is a suitable weight function. Note that the use of a weight function that decreases sufficiently rapidly with increasing radius is necessary to ensure that the sums are well-defined and are not dominated by the values of the PSF at large radii. The quantity $P_{total} = P_{xx} + P_{yy}$, which is invariant for rotations of the coordinates, is a measure of the square of the size of the PSF. A perfectly circular PSF will have $P_{xx} = P_{yy}, P_{xy} = 0$. Accordingly, the anisotropy of the PSF can be defined from its second-order moments as the quantity

$$\chi = (\chi_1, \chi_2) = ((P_{xx} - P_{yy})/(P_{xx} + P_{yy}), 2P_{xy}/(P_{xx} + P_{yy})) ,$$

where $\chi_1 \neq 0$ if the PSF is elongated along the x axis (>0) or the y axis (<0), while $\chi_2 \neq 0$ if the PSF is elongated along the positive diagonal (>0) or the negative diagonal (<0).

Image moments offer also a relatively straightforward way to measure the shape of an observed source. The moments of a source with light distribution I are defined as:

$$I_{xx} = \sum (x - I_x)^2 Iw \Big/ \sum Iw$$

$$I_{xy} = \sum (x - I_x)(y - I_y) Iw \Big/ \sum Iw$$

$$I_{yy} = \sum (y - I_y)^2 Iw \Big/ \sum Iw$$

in analogy to the above, the quantity $I_{total} = I_{xx} + I_{yy}$ is an estimate of the square of the source size. Kaiser et al. (1995) recommend the use of a circular Gaussian weight whose size is matched to that of the galaxy image itself:

$$w \propto \exp[-(x^2 + y^2)/2\sigma^2]$$

where the one-dimensional dispersion $\sigma = r_{half} / \sqrt{2 \ln 2}$ for a galaxy with half-light radius r_{half}. The source ellipticity e is then defined similarly to the anisotropy above:

$$e = (e_1, e_2) = ((I_{xx} - I_{yy})/(I_{xx} + I_{yy}), 2I_{xy}/(I_{xx} + I_{yy})),$$

A special case is the PSF-weighted ellipticity of the PSF itself, defined by replacing both the intensity I and the weight w in the above equations with the PSF P itself. This quantity has been used to quantify the anisotropy of the PSF in early versions of the JWST requirements; it has the advantage that all necessary definitions converge, while avoiding the need for externally defined quantities such as the center, scale,and functional form of the weight function. The magnitude and variation of the PSF-weighted ellipticity tracks the ellipticity changes that could be induced on the shape of external sources; see Casertano (2002) for further discussion.

If the anisotropy of the PSF is constant, it will be possible to determine it through an appropriate calibration program and largely correct it. To the extent that the PSF varies on time scales shorter than typical calibration programs, however, some residual effects will remain. Ground-based weak lensing studies currently use very large format cameras, so each image includes a large number of stars that can be used for an internal calibration of PSF variations. In contrast, typical NIRCam images are expected to include only a few tens of stars with sufficient signal to be used to calibrate PSF variations on an image-by-image basis; consequently, some degree of PSF stability will be needed to ensure successful weak lensing measurements.

5.0 Calculating the PSF

In this section, we look at analytical and numerical methods to calculate the PSF for simple optical systems. The analytical methods presented here are relatively simple, and are provided as a basis for understanding the theory behind the numerical calculations used in our JWST PSF simulations.

5.1 Fraunhofer Diffraction

Fraunhofer diffraction is a special case of diffraction theory in which the electric field ψ representing an incoming plane wave propagates through an aperture $A(x,y)$ and is then imaged at a location very far from the aperture itself (e.g, the “far field”). Specifically, Fraunhofer diffraction can be considered an approximation to the Fresnel-Kirchhoff diffraction integral,

$$\psi = -\frac{i}{2\lambda}\iint_A \frac{e^{ik(s+r)}}{rs}\left[\cos\theta_s - \cos\theta_r\right]dS,$$

for the limiting case when both the source and the point of observation are infinitely far from the aperture. In the above equation, the electric field strength ψ is determined by s, the distance from the source to a point (x,y) in the aperture plane, r, the distance from that point to a position in the image plane (u,v), and the wavelength λ. Here, the wavenumber k follows the conventional definition, $k \equiv 2\pi/\lambda$. We describe the angle between the source and the point in the aperture (relative to the normal of the plane of the aperture) by θ_s, and describe a similar angle formed between that same point in the aperture and the position in the image plane (again relative to the normal of the plane of the aperture) by θ_r.

For the case where both $s \to \infty$ and $r \to \infty$, the Fresnel-Kirchhoff diffraction integral for the electric field $\psi(u,v)$ in the image plane can be expressed as the Fraunhofer diffraction integral[10],

$$\psi(u,v) = C\iint e^{-ik(ux+vy)}A(x,y)dxdy,$$

where C is a constant of normalization. This expression is recognizable as a two-dimensional Fourier transform over the aperture. Thus in this limiting case, the observed electric field strength in the image plane can be obtained directly from the Fourier transform of the aperture distribution function itself. The resulting intensity distribution in the image plane – the PSF – is just the modulo square of the complex electric field, i.e. $|\psi(u,v)|^2$.

In a practical sense, the Fraunhofer approximation can be considered valid when the Fresnel number F satisfies the condition

$$F = a^2/\lambda r << 1,$$

where a is the diameter of the aperture and r is again the distance from the aperture to the image position. If this condition is not met, then the system is said to be in the Fresnel regime, where the equation for the field $\psi(x,y,z)$ is governed by the Fourier transform of the product of the complex electric field just outside of the aperture (e.g, the condition where $a^2/\lambda r \geq 1$) modulated by a quadratic phase exponential (Goodman 2005).

5.1.1 Analytical Calculations of the PSF

In the Fraunhofer approximation, it is relatively straightforward to calculate the intensity distribution of the PSF analytically, assuming the aperture function *A(x,y)* is not terribly complicated.

[10] The derivation of the Fraunhofer diffraction integral from Fresnel-Kirchhoff diffraction integral is a classical derivation in the field of optics, the details of which are elegantly described by Born and Wolf (1999). Another derivation based on the Huygens-Fresnel principle, is provided by Goodman (2005).

5.1.1.1 The Square Aperture

Probably the simplest case to consider is the rectangular aperture, described by the two-dimensional function

$$A(x,y)=^2\Pi(x,y) = \Pi(x)\Pi(y), \quad where \quad \Pi(x) = \begin{cases} 1 & |x| < 1/2 \\ 0 & |x| > 1/2 \end{cases}$$

Here we have used the formalism of Bracewell (2000) to describe the "rectangle function" $\Pi(x)$. If the aperture is illuminated by a unit-amplitude, monochromatic plane wave, then the distribution of the electric field $\psi(u,v)$ in the image plane is given by the Fourier transform of the aperture function itself, e.g.

$$\psi(u,v) = C\ \mathrm{sinc(u)sinc(v)}$$

where C is once again a constant of normalization. The PSF resulting from this aperture is therefore $I(u,v) = |\psi(u,v)|^2 = C^2\ \mathrm{sinc}^2\mathrm{(u)}\ \mathrm{sinc}^2\mathrm{(v)}$.

5.1.1.2 The Circular Aperture

A more familiar example is the circular aperture of radius r. As with the square aperture above, we can describe this aperture using Bracewell's rectangle function, e.g. $A(r) = \Pi(r)$. Because of radial symmetry of the aperture, we can rewrite the two-dimensional Fourier transform in the Fraunhofer diffraction integral as a Fourier-Bessel (or Hankel) transform,

$$\psi(u,v) = 2\pi \int_0^\infty \Pi(r)\ J_0(2\pi qr)\ r\ dr$$

where $J_0(2\pi qr)$ is a zeroth-order Bessel function of the first kind. Solving for the integral yields

$$\psi(u,v) = {J_1(\pi q)}\big/{2q},$$

where $J_1(\pi q)$ is a first-order Bessel function of the first kind[11]. Thus it follows that the PSF for a circular aperture is again the square of the electric field, or

$$I(u,v) = |\psi(u,v)|^2 = \left[\frac{J_1(\pi q)}{2q}\right]^2,$$

which is often referred to as the Airy Function.

It is worthwhile to note that the PSF of most any aperture function that can be expressed analytically can also be calculated using expressions like those noted above. However, as we show in the following sections, the structure in the PSF for even a moderately

[11] Bracewell (2003) defines the function *jinc q* such that $jinc\ q \equiv {J_1(\pi q)}\big/{2q}$

complicated aperture would be a serious challenge to do analytically. In such circumstances, numerical methods to calculate the PSF are beneficial.

5.2 Impact of the Pupil Shape on the PSF

To lowest order the PSF of an imaging system is determined by two things: the pupil shape and the wavefront errors. Often, the shape of the pupil is well known and relatively simple, as in the case of a circular or annular aperture. However, more complex pupils are increasingly common for large systems (the JWST and Keck pupils are prime examples). Errors in the wavefront can arise from a variety of sources, including imperfections in the system's optics (which tend to be static or semi-static) or atmospheric variations (as in the case for ground-based observations), and can be extremely difficult to determine. Here, we illustrate how the pupil shape affects the PSF, building from an open circular pupil of diameter ~6.5 m (Figure 4a) and proceeding in steps towards a realistic representation of the JWST pupil (Figure 4e).

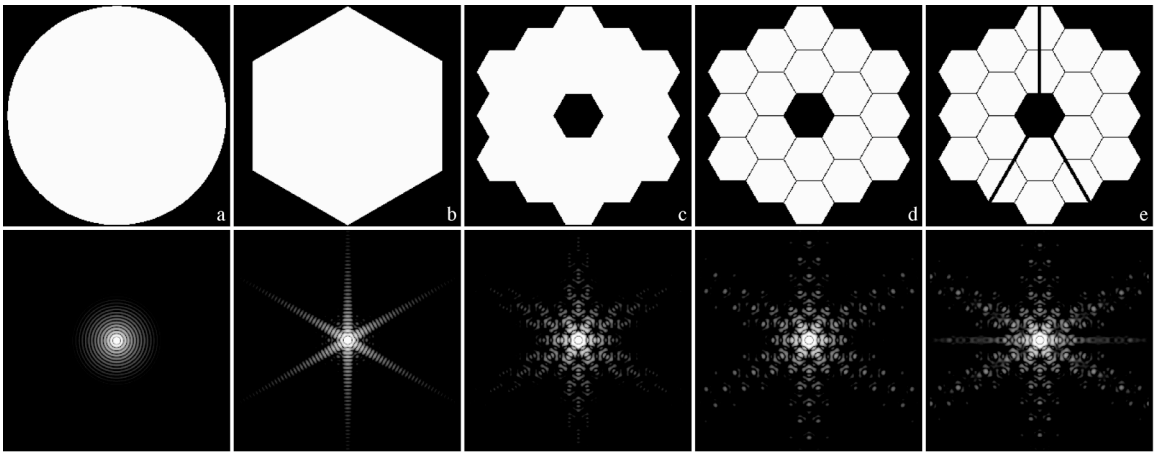

Figure 4: A series of model telescope exit pupils (top), with their corresponding Point Spread Functions (bottom). All PSFs shown are displayed on the same logarithmic grayscale, with minimum and maximum pixel values of 3.0e-7 and 3.0e-4 respectively. PSFs have been normalized such that the total number of counts for each PSF is 1.

For the following discussion, we have generated PSFs using JWPSF with an input pupil of size 1024 x 1024 pixels, representing a 6.5 m diameter along the longest dimension. In all cases, we have assumed $\lambda = 2\ \mu m$, with no OPD errors (as such, by definition, each of these PSFs has a Strehl ratio of unity). All resulting PSFs are shown on the same logarithmic intensity scale, with minimum and maximum pixel values of 3.0×10^{-7} and 3.0×10^{-4} respectively. PSFs are shown on a 4x oversampled pixel scale. The sharpness has not been computed, since it is only meaningful for the PSF resampled to detector pixels.

As discussed in Section 5.1.1.2, the Fourier transform of a circular pupil (Figure 4a) is just the Airy function, as shown in the PSF below Figure 4a. Moving to a hexagonal input pupil (Figure 4b) imparts a hexagonal symmetry to the PSF pattern, and in particular creates diffraction spikes at 60 degree intervals bisecting the angles of the hexagon. When compared with the ideal circular aperture, the hex PSF's FWHM

increases significantly (~10%), as does the radius to the first diffraction ring (from 0.079 arcsec to 0.086 arcsec). The percentage of energy within 50 mas of the center decreases by 4.5%, though there is little change to the percentage of flux scattered beyond a radius of 1 arcsec.

The third pupil (Figure 4c) introduces the "tricontagon" outline of the JWST Primary Mirror, along with the hexagonal "missing segment" at the center of the mirror (the occulting area of the Secondary Mirror fits within this region). While the symmetry of the hexagonal pupil's PSF is maintained, the overall PSF pattern is significantly more complex (a "snowflake" pattern). The full width at half maximum and the radius of the first diffraction ring are slightly smaller than for the open hexagon (0.067 arcsec and 0.080 arcsec respectively), but the percentage of flux within a 50 mas radius has decreased to 68%, while the flux outside of 1 arcsec has increased to 1.2%, reflective of the increased mid- and high-spatial frequencies in the pupil.

Table 1: Comparison of Typical PSF Properties with Pupil Shape for λ = 2 μm (OPD = 0)

Shape	Peak Pixel Intensity†	FWHM (arcsec)	Radius of first minimum (arcsec)	Percentage Flux				Ellipticity Parameters		
				within first minimum	within 50 mas	within 150 mas	outside 1 arcsec	e1	e2	Total
Circle	0.0141	0.064	0.079	84.4	79.1	91.7	0.8	0.0000	0.0000	0.0000
Hexagon	0.0117	0.070	0.086	83.9	74.6	91.0	0.9	0.0060	0.0000	0.0060
Tricontagon Outline	0.0112	0.067	0.080	74.2	68.1	88.9	1.2	-0.0043	0.0000	0.0043
Tricontagon w/gaps	0.0101	0.069	0.083	72.4	65.3	87.0	1.8	-0.0025	0.0000	0.0025
JWST Pupil	0.0105	0.067	0.080	70.8	64.9	85.6	2.8	-0.0145	0.0000	0.0145

In the fourth pupil (Figure 4d) we introduce the segment gaps to represent the eighteen hexagonal mirrors that comprise the JWST Primary Mirror. As with the previous pupil, an increase in the mid- and high-spatial frequencies over the pupil have increased the complexity of the resultant PSF, diffracting more flux from the PSF core to larger radii. Here, an additional ~3% is lost from the central area of radius 50 mas relative to the tricontagon pupil, and flux scattered beyond 1 arcsecond increases to 1.8%.

The last pupil (Figure 4e) includes both the mirror segment gaps and the obstruction due to the Secondary Mirror support structure. The addition of the Secondary Mirror supports generates three "diffraction bars" in the PSF normal to the direction of the supports in the pupil. The horizontal bar can be clearly seen cutting through the mid-plane of the PSF, but the other two are coincident with the diffraction spikes at $\pm 60°$. Surprisingly, the model predicts a slight increase in the intensity at the central pixel (presumably due to the coincidence of the bars with the PSF center), though the fraction of flux contained within both the first diffraction ring and within a 50 mas radius has

decreased by 1.6% and 0.4% relative to the previous pupil. The strongest effect is seen in the energy scattered outside the 1 arcsecond radius which increases by about 1%. When compared with the Airy pattern from the circular pupil, we calculate a loss of ~14.2% of the flux within a radius of 50 mas and a corresponding 2.0% increase in the flux scattered outside of 1 arcsec.

The hexagonal symmetry to the perfect JWST PSF is not unique. For example, the twin 10 m diameter Keck telescopes also produce a complicated, hexagonal PSF resulting from its thirty-six hexagonal primary mirror segments. However, many of the detailed features of the Keck PSF are smeared out by the atmospheric distortions of the wavefront. JWST may be the first observatory in which astronomers will be sensitive to the impacts of the segmented mirror design on the shape of the PSF.

For comparison, we show the nominal HST pupil and its resultant PSF in Figure 5. Even without the presence of 0.5 waves RMS of spherical aberration (at $\lambda = 0.5\ \mu m$), the Hubble PSF would have shown a complicated structure, due primarily to the combined diffractive effects of the secondary mirror support structure and the three circular mirror pads holding the Primary Mirror in place.

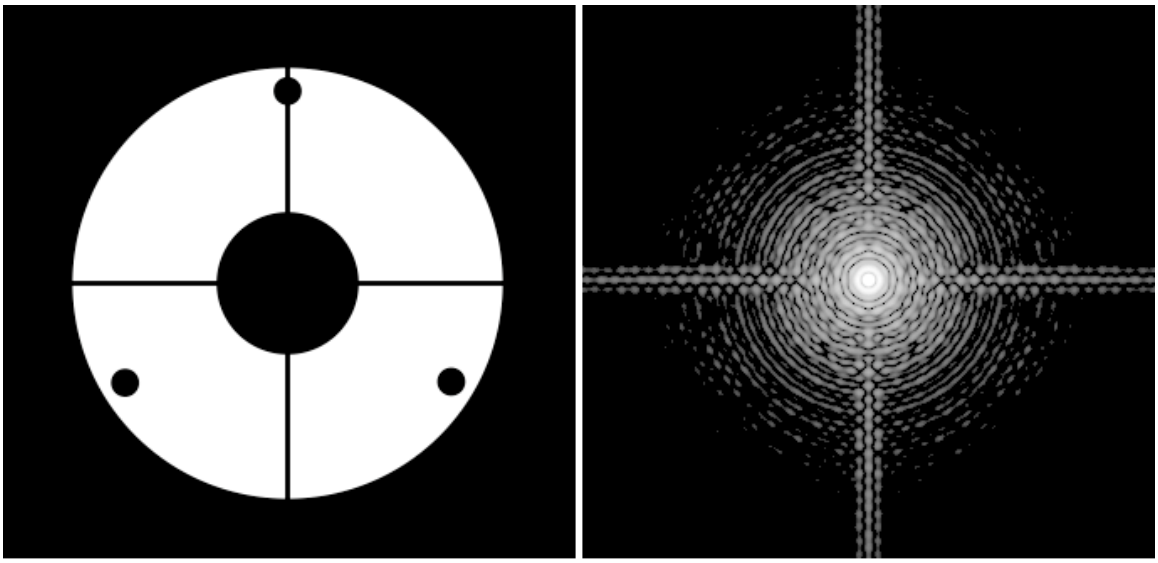

Figure 5: Nominal exit pupil for the 2.4 m diameter HST (left) and its resultant PSF (right). Note the combined diffraction pattern due to the secondary mirror supports and the three circular mirror pad obscurations. The PSF is displayed logarithmically with minimum and maximum pixel values of 3.0e-7 and 3.0e-3 respectively.

6.0 PSF dependence on wavelength

As described in the previous Section, the PSF generated by a telescope such as JWST, with its irregularly-shaped pupil, deviates from the perfectly shaped Airy function of an unobstructed circular aperture. However, in the absence of wavefront errors, as in the idealized case discussed there, the properties of the PSF do not change qualitatively as a

function of wavelength. The PSFs depicted in Figure 4 will increase in size proportionally with wavelength, but otherwise maintain the same shape. In practice, detector effects cause the PSF ultimately delivered to the science user to deviate from this ideal behavior; JWST will be ideally (Nyquist) sampled at 2 μm, with two pixels across the FWHM, but will be significantly undersampled at shorter wavelengths – a situation familiar to many users of HST instruments.

Optical imperfections, whether due to aberrations inherent in the optical design (*design residuals*) or to misalignments and figure errors in the optical train, will drastically change the PSF behavior as a function of wavelength. Optical imperfections can be treated as phase errors across the pupil of JWST – essentially an image of the primary – as described in Optical Path Difference images (see the right panel in Figure 2). Such phase errors affect PSFs at shorter wavelengths to a much larger degree, especially when the total wavefront error, measured as the root mean square phase error across the pupil, exceeds λ/14 (the nominal "diffraction-limited" criterion). For the nominal JWST optical error budget, the nominal diffraction limit is violated at wavelengths shorter than 2 μm.

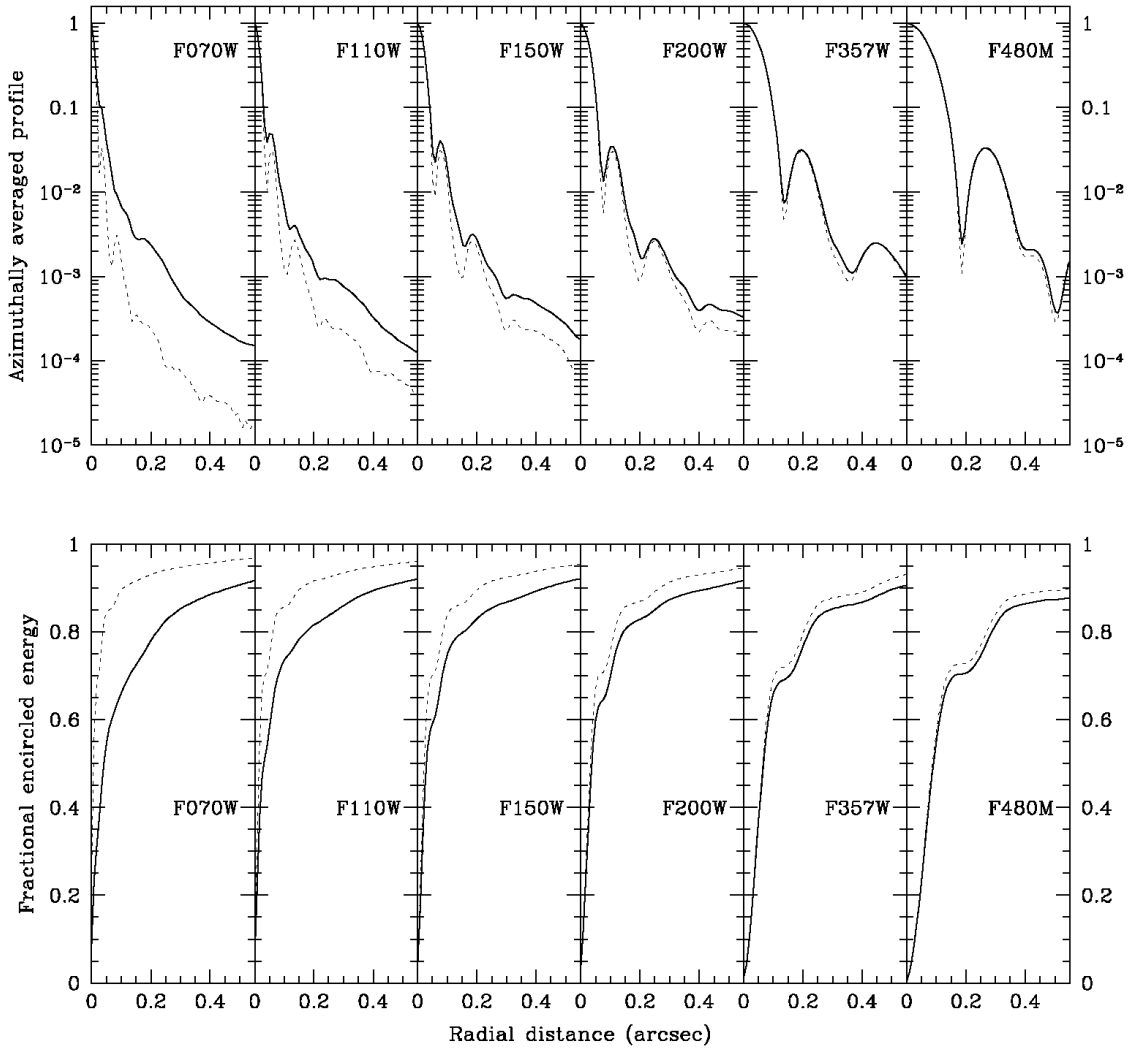

Figure 6: Azimuthally averaged profile (top) and encircled energy (bottom) for representative PSFs in several NIRCam filters. The dashed lines show PSFs with the correct pupil function, but no wavefront errors; the solid curves show PSFs obtained assuming wavefront errors consistent with the Revision T error budget. The radial profiles are scaled to unit central value.

Quantitatively, these differences are shown in Figure 6. The top row shows the azimuthally averaged profile for broad-band PSFs at wavelengths ranging from 0.7 to 4.8 μm (filters F070W through F480M). The dashed line shows the profile for a PSF without wavefront errors, while the solid line uses a representation of the phase errors that may be typical of a well-performing JWST (based on the Revision T error budget). The bottom row shows the fractional encircled energy for the same PSFs. At shorter wavelengths, the central core is sharper, and the PSF is close to the ideal case within the central 20 mas; however, the profile deviates progressively more from the ideal case at radii of 0.1" or larger. At wavelengths longer than 2.0 μm, the PSF approaches the ideal case even beyond 0.2". At large radii, this results in short-wavelength PSFs enclosing less energy than longer-wavelength ones. For example, the 2.0 μm PSF has about 81% of the light

within 0.15", while the 0.7 μm PSF has only about 72% - the nominal values without phase errors are 85% and 91%, respectively.

As we shown in Figure 7, the wavelength dependence of key PSF properties varies in a predictable manner. Here, we present two PSF measurements of astronomical interest: the fraction of the total flux within a 0.15" radius, and the FWHM, both measured on simulated broad-band PSFs for filters F070W through F480M. We notice that the total flux within the 0.15" radius shows a peak around 2.0 μm, the shortest wavelength where the PSF is truly diffraction-limited. At wavelengths shorter than 2.0 μm, the impact of wavefront errors pushes an increasing fraction of the light towards larger radii; at longer wavelengths, the PSF increases in size, offsetting the relative reduction in WFE at these wavelengths. Conversely, when we examine the PSF FWHM – as determined by Gaussian fitting to the PSF core – we see that the FWHM scales roughly with wavelength. This quantity depends primarily on the inner regions of the PSF, and is dependent on the size of the pupil and the wavelength of observation, and is not affected by wavefront errors as much as the encircled energy.

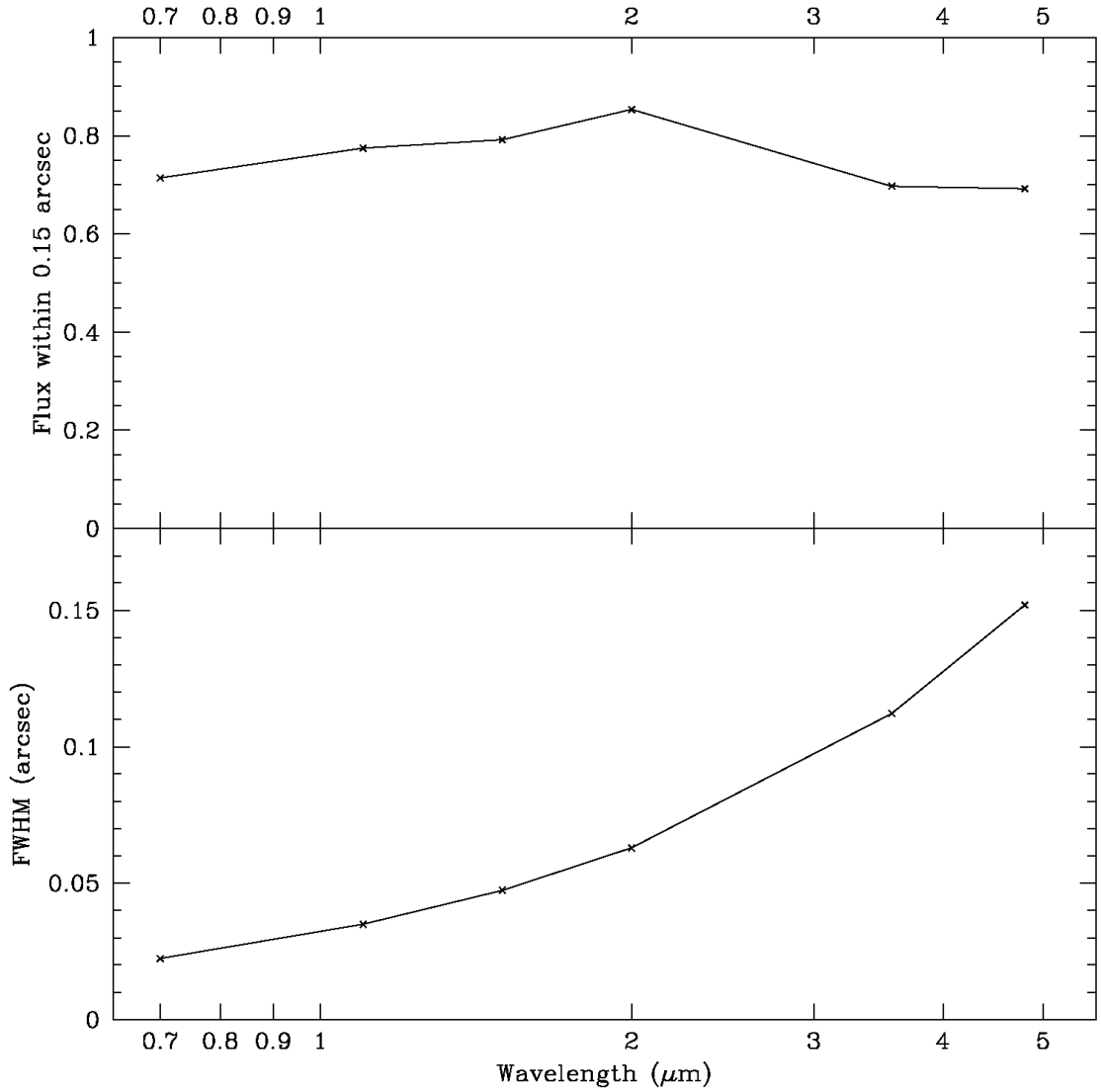

Figure 7: Wavelength dependence of PSF properties. (Top) fraction of the total flux within a 0.15" radius. This quantity peaks around 2 micron, which is the shortest wavelength where the PSF is truly diffraction-limited. At shorter wavelengths, the impact of wavefront errors pushes an increasing fraction of the light towards larger radii; at longer wavelengths, the PSF increases in size. (Bottom) FWHM of the PSF, determined by Gausian fitting to the PSF core. This quantity depends primarily on the inner regions of the PSF, within its nominal Airy size, and scales roughly with wavelength, and is not affected by wavefront errors as much as other quantities. Note that this FWHM is measured in an oversampled representation of the PSF; in practice, due to PSF undersampling its measured FWHM will be larger than indicated here at the short wavelength end (< 1.1 μm).

6.1.1 Comparison with other missions

In order to appreciate the scientific impact of JWST, it is useful to compare its expected performance with other telescopes, especially space-based. The obvious comparisons are HST in the visible and very near IR and Spitzer in the IR.

Although JWST is principally an IR telescope, and it does not satisfy the diffraction-limited criterion shortward of 2 μm, its optical performance even at short wavelengths is scientifically very appealing. The FWHM at 0.7 μm is predicted to be approximately 0.03", smaller than the pixel size; even after including pixelation effects, the PSF core is likely to be significantly sharper than in ACS/HRC, with a measured FWHM of 0.07" (ACS Instrument Handbook). Similarly, the radius including 50% of the flux is smaller than in ACS (Table 2; ACS data from Sirianni et al. 2005), although the gain is not as significant because of the increasing impact of wavefront errors. A similar comparison with NICMOS is more difficult, since the large-radius PSF for NICMOS is not as well characterized. For NIRCam, 50% of the flux at 2.0 μm is expected within a radius of 0.043"; with NICMOS Camera 2 at F160W, half the light *within 0.75"* is enclosed within a radius of 0.070" (Holfeltz & Calzetti 1999). Even including estimated pixelation effects, JWST images in the red part of the visible spectrum will exceed significantly those delivered by HST, not only in depth but also in resolution. For studies that depend on PSF size, such as stellar populations in nearby galaxies or Cepheid variables beyond Virgo, JWST will deliver an improvement in speed by over a factor 10 even in R and I.

Table 2: Radii corresponding to given encircled energy fraction – HST and JWST

Fraction	0.7 mm		2.0 mm	
	HST (ACS HRC F814W)	JWST	HST (NIC2 F160W)*	JWST
40%	0.05"	0.040"	0.050"	0.033"
50%	0.07"	0.055"	0.070"	0.043"
60%	0.10"	0.085"	0.125"	0.068"

* Note: NICMOS measurements are as fraction of total light within a radius of 0.75", rather than to infinity.

Beyond 2 μm, the natural comparison is with Spitzer, which covers the wavelength range from 3.5 to 140 μm, but has been especially effective up to 24 μm. The Spitzer mission has been extremely successful and has opened new vistas in the mid- and thermal infrared, primarily thanks to its extremely low background and relatively large field of view – this with a mere 85 cm mirror. In many ways, the primary limitation of Spitzer is its modest angular resolution – at 24 μm, with a FWHM of approximately 6", the confusion limit is reached in a few hours of integration, thus limiting the effective sensitivity of the telescope. JWST will cover the range of wavelengths most used in Spitzer imaging, and will be essentially diffraction-limited in this range. Thanks to its 8x smaller PSF, JWST will improve its sensitivity to point sources and unresolved objects by a factor of *several thousand* over Spitzer, thanks to both the larger collection area and the smaller region of the sky that contributes to the noise.

Figure 8: A comparison between the Spitzer (left) and simulated JWST (right) observations of the Hubble Ultra-Deep Field (HUDF). The Spitzer/IRAF images comprise 25 hours of exposure of a 1' x 1' region of the HUDF in channels 1 (3.6 μm), 2 (4.5 μm) and 3 (5.8), obtained as part of the GOODS Spitzer Legacy Project. The simulated JWST NIRCam images assume 1000 s of integration at bandpasses similar to those observed by Spitzer.

We present in Figure 8 a comparison of simulated JWST images with actual Spitzer images of the Hubble Ultra-Deep Field, and present a similar comparison between simulated JWST images and ACS images of the same field in Figure 9. The comparison between ACS and JWST, kindly made available by Massimo Stiavelli, shows that JWST can achieve depth and resolution in the near-IR that is better than HST can achieve in the visible. The comparison with the Spitzer image shows the dramatic improvement that JWST can achieve *in 1000s of observation* in comparison with some of the deepest image Spitzer has obtained with IRAC, a total of 90,000s of exposure in the deep GOODS field.

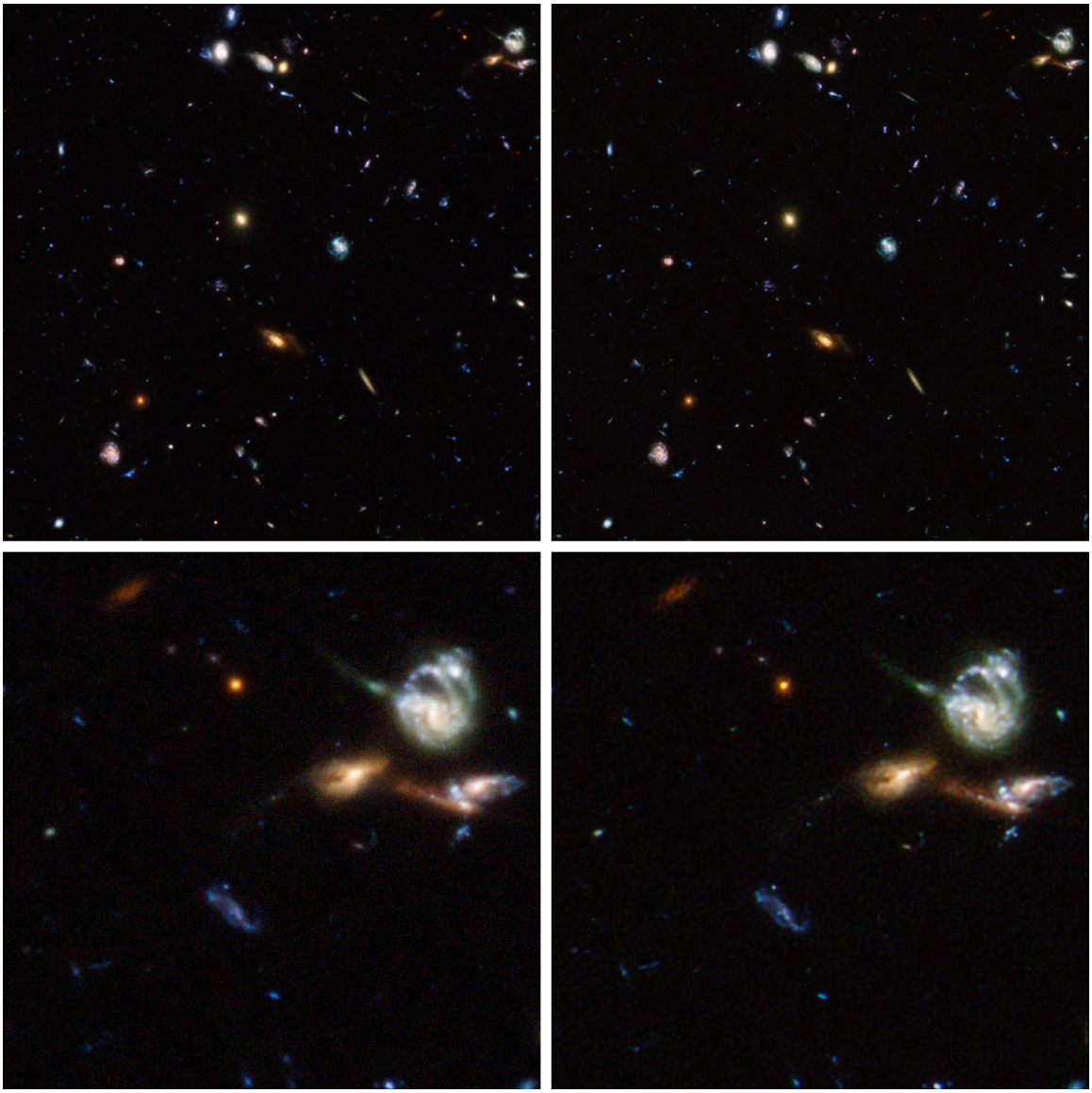

Figure 9: ACS image of the HUDF field (top left) in V-, I-, and Z-band, compared with a simulated JWST/NIRCam image in F0707W, F090W, and F115W (top right). A 500 x 500 pixel detail of the galaxy group in the upper-right of the field is shown beneath each image. Even though JWST is not optimized for optical observations, its large primary mirror produces a PSF that is small enough to compare favorably with HST/ACS imaging.

In Figure 10 we present a similar comparison between simulated JWST images and NICMOS images of the HUDF field, also made available to us by Massimo Stiavelli. Not surprisingly, the depth and resolution JWST will achieve in the near-IR far surpasses the capabilities of HST's NICMOS at these wavelengths.

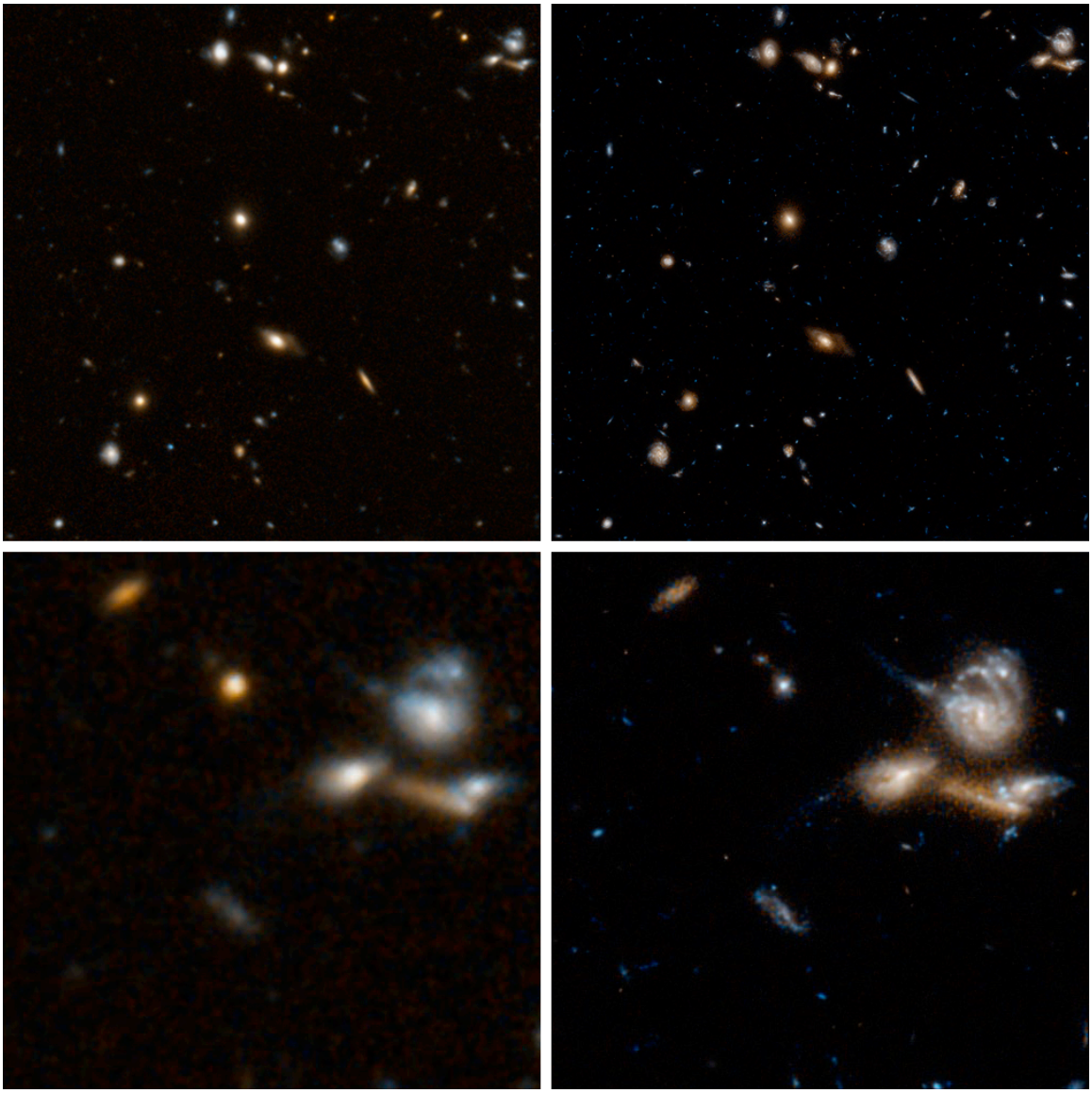

Figure 10: NICMOS image of the HUDF field (top left) in the J-, H-, and K-bands, compared with a simulated JWST/NIRCam image through similar bandpasses (top right). A 500 x 500 pixel detail of the galaxy group in the upper-right of the field is shown beneath each image.

7.0 PSF Dependence on error budget realization

In order to quantify the impact of expected variations of the PSF over time, we consider a number of different realizations of the JWST PSF provided to us by the JWST Project. These PSFs differ in the specific distribution of the wavefront error across the pupil; all satisfy, in a statistical sense, Revision T of the wavefront error budget, both in total rms wavefront error and in its distribution as a function of wavenumber (cycles across the pupil). As long as the error budget is satisfied, comparing these PSFs provides *an upper limit* to the PSF differences that could be encountered in the normal course of

observations; the reason is that some wavefront errors, primarily higher frequencies and those arising inside NIRCam, are likely to be highly correlated between different times, and therefore using completely independent realizations can overestimate the temporal variation in the properties of the PSF (see Figure 11). A more realistic estimate of PSF variations can be obtained from finite element modeling of telescope changes (e.g., the SDR4 effort); however, such PSFs are not yet available to us. For our present purposes, using the changes that are allowable within the parameters of the total wavefront error budget provides a useful estimate of the magnitude of changes that might be expected, especially since many of the large changes in PSF properties are closely related to the low-order aberrations, which most likely *will* vary on a short time scale.

We consider explicitly two filters: F070W, the shortest wavelength broad-band filter on NIRCam, and thus most likely the most affected by wavefront errors; and F200W, where the PSF is nominally diffraction-limited in NIRCam. We expect that differences between PSFs, especially for what concerns the OTE contribution to the wavefront error, will become smaller and less meaningful at longer wavelengths. For each of these filters, we produced 10 different PSFs with the exact same pupil function but different realizations of the wavefront error budget.

In Figure 11 we show two of the OPD maps and their corresponding PSFs (produced with JWPSF) at 4x oversampling at a wavelength of 2.0 μm. These OPDs were produced using the Rev T optical error budget, and assume WFE allocations (including reserves) for the OTE, ISIM, and NIRCam. The RMS WFE of the OPD at the left is 110.3 nm, while the RMS WFE of the OPD at the right is 109.6 nm over the clear area of the pupil. While the differences in total RMS WFE are small, the impact of these differences on the resultant PSFs is measurable. For example, the core of the simulated PSF at the left in Figure 11 shows a noticeable triangular shape, while the PSF at the right of Figure 11 shows a more circular geometry. While these differences are easily apparent with the lack of noise and oversampling used in these simulations, distinguishing small PSF variations when sampled using NIRCam detector pixels for on-the-sky targets may require a more expert analysis. In the end this may be a practical limit on the use of PSF knowledge for the types of science described in Section 2.0. Figure 12 compares the PSFs for F070W and F200W for the same OPDs presented in Figure 11 (but on a slightly different grayscale). There are considerable differences between the two sets of PSFs, with the F070W PSFs showing more structure and asymmetry than the F200W PSFs.

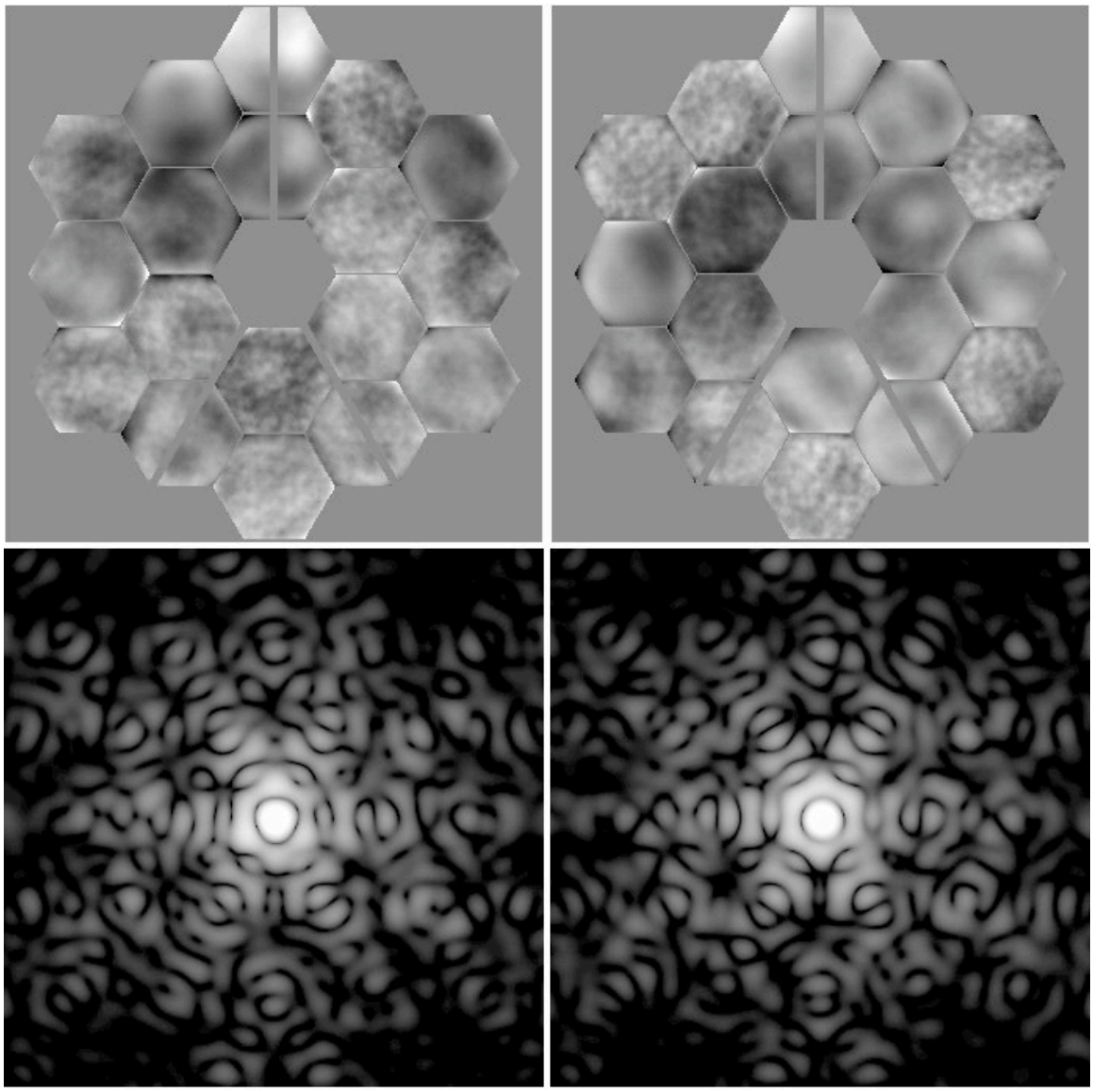

Figure 11: Comparison of two JWST Rev T OTE error budget OPDs (top) and their associated PSFs (bottom) for a wavelength of 2.0µm. OPDs are displayed on a linear grayscale from -400 to 400 nm, while PSFs are displayed on a logarithmic grayscale from 1.0e-6 to 1.0e-3. The OPDs include WFE contributions from the OTE, ISIM, and NIRCam. The RMS WFE of the OPD at left is 110.3 nm, while the RMS WFE of the OPD at right is 109.6 nm. While the differences in total RMS WFE are small, the impact of these differences on the resultant PSFs is measurable.

We processed the PSF in F070W and F200W, for each of the ten OPD realizations, in the same way. We computed several standardized quantities for each, as well as the cross-PSF quantities described in Section 4.3. The sharpness is computed in detector pixels, binning the oversampled PSF into the planned output pixels without considering sub-pixel sensitivity variations; only pixels within 0.15" of the nominal PSF position are considered. The ellipticities are computed using the PSF itself as weight, as described in Section 4.4. We present the variations in the global properties for the F070W and F200W PSFs in Table 3. It is apparent that global, non-directional quantities, such as

size, sharpness, and flux fraction within 0.15", vary only modestly for different PSF realizations; such PSF properties can be well characterized by any one of the different realizations available to us. On the other hand, the ellipticity of the PSF varies substantially across realizations, especially at the shorter wavelength where the typical (rms) ellipticity is 15% per component, while the systematic component is a factor of several smaller. The ellipticity at F200W is substantially smaller, about 2% systematic and 3% random.

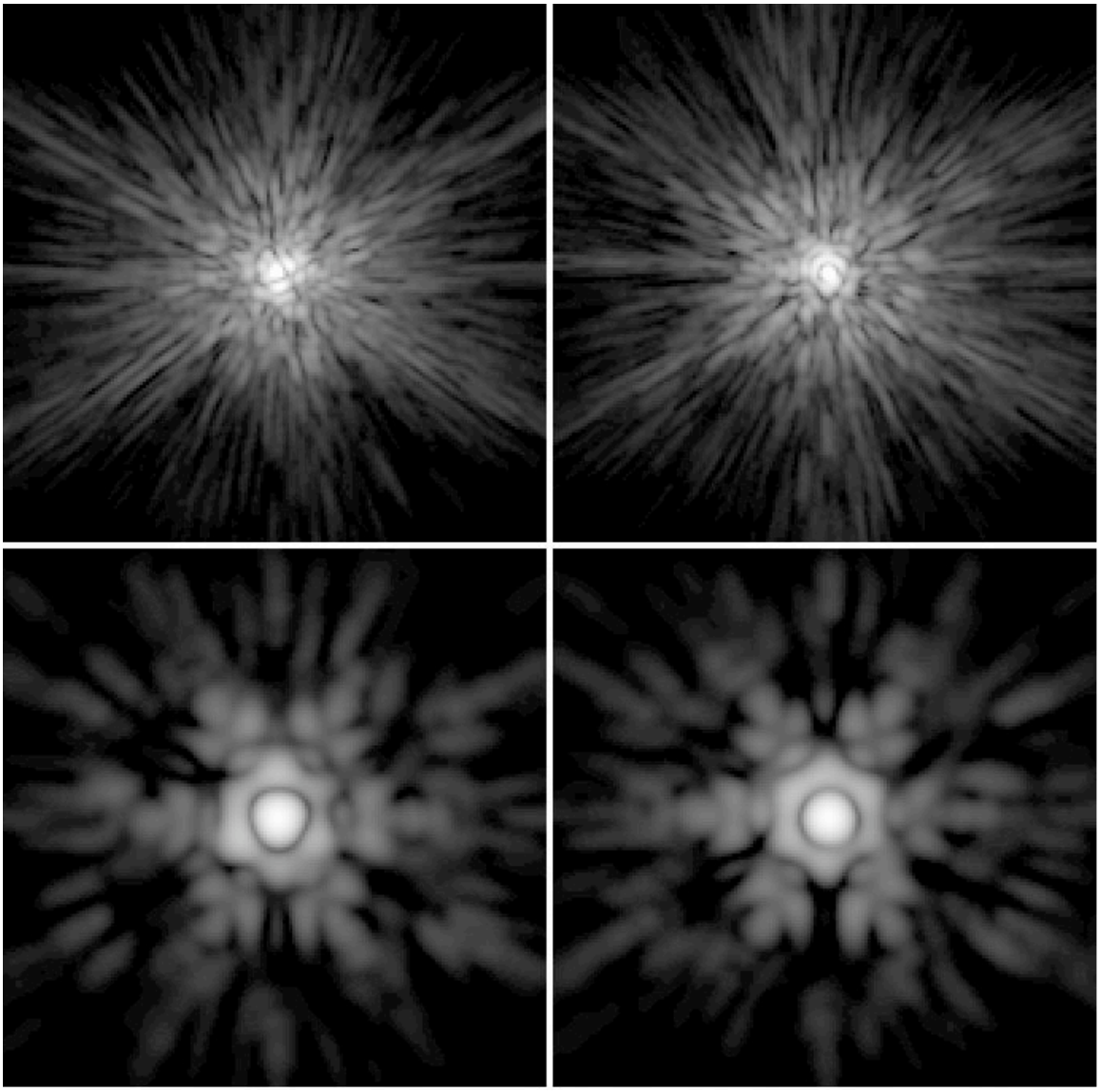

Figure 12: Comparison of PSFs from the same two Rev T OTE error budget OPDs shown in Figure 11 for the F070W (top) and F200W (bottom) broadband filters. These PSFs are presented on the same (angular) pixel scale, and displayed on a logarithmic grayscale from 1.0e-6 to 1.0e-2. Many of the asymmetries apparent in the F070W PSFs are no longer apparent in the F200W PSFs, though considerable differences between the two sets of PSFs still remain.

Table 3: Variations in global PSF properties

	Sharpness		Flux inside 0.15”	Ellipticity	
	mean	min, max		e1	e2
F070W	0.155 ± 0.026	0.107, 0.194	0.72+/-0.01	0.046+/-0.154	-0.031+/-0.147
F200W	0.076 ± 0.002	0.073, 0.082	0.80+/-0.01	0.014+/-0.024	-0.010+/-0.030

In Section 4 we also introduced two quantities that characterize the detailed variation of the PSF as a function of realization, namely the cross-correlation between PSFs and the maximum residual in the annulus between 0.05” and 0.15” after PSF subtraction. Unlike sharpness and enclosed flux, the cross-correlation and the PSF residuals are directional, in that they can be affected by PSF variations that do not change its azimuthally-averaged profile. The cross-correlation between PSFs is an indication of how much uncalibrated PSF variations can affect PSF-fitting photometry; the subtraction residuals indicate the magnitude of spurious sources that might be identified as a consequence of imperfect PSF subtraction.

As might be expected, both cross-correlation and residuals are much better behaved in F200W than in F070W. Cross-correlation between realizations average 93% in F070W, meaning that without calibration, the flux of a point source will be underestimated by 7% on average when using PSF fitting, with a dispersion of 12%. In F200W, the average is very close to unity for this specific set of realizations, so that there is no systematic bias; however, the rms error is about 5%. The maximum subtraction residuals between 0.05” and 0.15” average about 6% of peak in F070W and 4% in F200W. Details are given in Table 4.

Table 4: Cross-correlation and maximum subtraction residuals across PSF realizations

	Cross-correlation				Residual (max pixel/peak)			
	Avg	Rms	Min	Max	Avg	RMS	Min	Max
F070W	0.973	0.121	0.716	1.201	0.057	0.022	0.015	0.116
F200W	0.997	0.049	0.881	1.130	0.042	0.012	0.017	0.065

To the extent that the differences among the PSF models available to us are representative of in-flight variations, the clear indication is that PSF-fitting photometry to better than 10% (5%) in F070W (F200W) requires careful calibration of the PSF, from the science data themselves if possible; the same is true of shape measurements and of PSF modeling to detect faint sources within 0.15” of a bright point source.

8.0 Multiple approaches to PSF modeling

It is apparent that there are many different ways to estimate and calculate a predicted PSF for JWST. The different advantages of the approaches presented here will make it possible to tailor the model to the specific needs of each study, and eventually of the end user. Highly complex, high-fidelity models (CODE V, etc) are suitable to predict in

detail much of the expected wavefront error in a realistic system, but may be outside of the reach of most scientists. ZEMAX models are more portable thanks to the broader availability of the modeling software; once such models have been developed to a similar level of fidelity, they might serve as the intermediate link to the advanced end user. PROPER includes physical wave propagation that might be critical for a full understanding of coronagraphic performance or for high-dynamic range imaging without coronagraphy. The interface provided by JWPSF permits an accurate calculation of the PSF for a variety of scientific calculations, including realistic consideration of source spectra and system throughput, once the relevant wavefront error images have been computed via more advanced software. Some of these methods overlap in either scope or availability, but much progress is still needed in the understanding of both modeling approaches and JWST properties before a broad suite of tools suitable for general use is finalized.

Even in their current, evolving state, the variety of available methods can be combined to explore questions that would not be accessible to individual methods. As an example, we illustrate how the monolithic ZEMAX OTE model and JWPSF can be combined to determine the effect of low order aberrations, due for example to small motions or misalignments of the secondary mirror, on the properties of a realistic PSF (see the top row of Figure 13). First, the monolithic model is used to determine the wavefront error for the nominal configuration. Then, the desired small motion (in the case of Figure 13, 0.2 waves of defocus) is applied, and the resulting wavefront error is obtained. Then, the *difference* in the wavefront error images is added to one of the wavefront error images used by JWPSF, after resampling to the appropriate grid if needed. Finally, the combined wavefront error is fed to JWPSF with the desired source properties in order to obtain the predicted PSF. While not perfect, this method permits a good analysis of the impacts of mirror misalignments on the properties of the PSF, in a way that is potentially accessible to users without expensive modeling tools.

For comparison, we produced a similar calculation with PROPER using the same input OPD file used by JWPSF (see the bottom row of Figure 13). Instead of using the ZEMAX-determined wavefront error corresponding to 0.20 waves of defocus, we applied a defocus term of 0.15 waves RMS (using an obscured circular Zernike calculation) directly to the wavefront using tools available in PROPER. We found little apparent difference in the resultant PSFs generated using the two methods, despite the difference in the specified defocus term (z_4). An investigation into this discrepancy has suggested differences in the Zernike normalizations between the ZEMAX and PROPER calculations as a potential reason for the similar result despite the variations in input.

We note that the PROPER calculation was set up to mimic the JWPSF calculation as much as possible, e.g. with a wavefront from a single optical element (the primary mirror) converging to a focus in the far field. We expect differences between JWPSF and PROPER-generated PSFs to be more pronounced once we enhance the PROPER model to propagate a wavefront from optic to optic, including the JWST Primary, Secondary, Tertiary, and Fast Steering Mirrors. We intend to perform a detailed quantitative comparison of the different modeling approaches in future studies. Similar techniques

can eventually be used with other accessible tools in order to predict various aspects of the scientific performance of JWST.

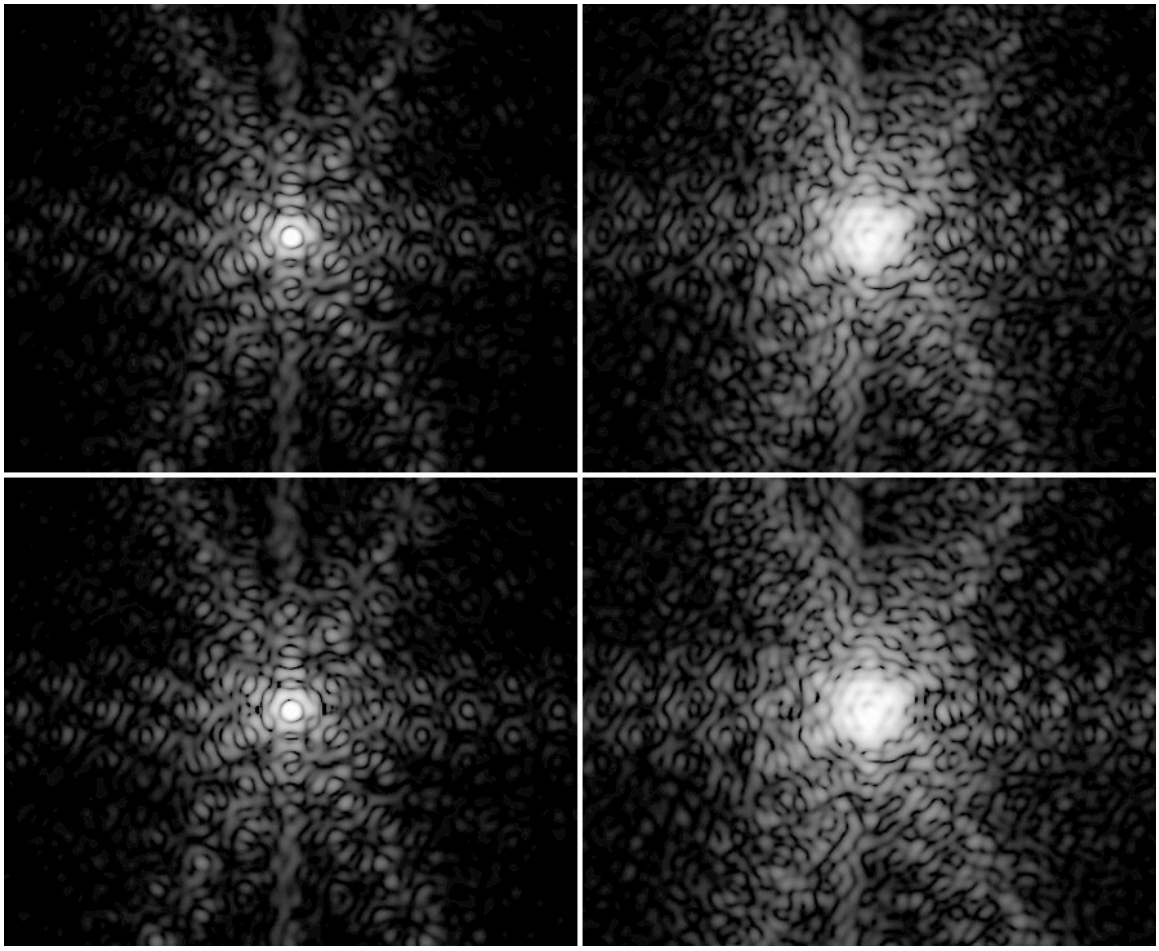

Figure 13: Narrow-band PSFs modeled in F187N obtained with JWPSF (top) and PROPER (bottom) from one of the Rev T OPD error realizations. At left is show the central regions of each PSF, calculated using the Fourier Transform method (JWPSF, top) and the angular spectrum method (PROPER, bottom). At right we show the result of adding 0.20 waves of defocus to the Rev T OPD. Top Right: JWPSF-generated PSF produced after adding the defocus predicted by a ZEMAX model with a monolithic JWST primary mirror (top, see Section 3.2.1). Bottom Right: PROPER-generated PSF produced by applying an obscured circular Zernike corresponding to 0.15 waves RMS of defocus to the OPD.

9.0 Conclusions

A good, stable PSF is critically important to the goals of many of the science projects envisioned with JWST. Previous experience with other space telescopes, including HST, has shown that the ability to obtain groundbreaking discoveries relies heavily on the quality and the understanding of the telescope's PSF. However, unlike the HST PSF, which shows variations in focus on orbital and secular timescales due primarily to thermal variations in focus length, the JWST PSF will undoubtedly show more complicated behavior. With 18 semi-rigid primary mirror segments, each with 7

controllable degrees of freedom, and a secondary mirror with an additional 6 degrees of freedom, the JWST PSF can vary with at least 132 degrees of freedom.

Though a wavefront sensing and control system will allow for correction of misalignments in the primary mirror segments and secondary mirror, ensuring that the PSF never exceeds its total RMS wavefront error (WFE) of 131 nm, there remain an infinite number of different PSFs that fit within this error budget. Since there exists considerable potential for thermal variations between mirror updates, PSF variability is likely, even if the PSF stays within its WFE budget at all times. Understanding slight variations in the properties of the PSF over both short and long timescales will be critical to achieving the science goals with JWST.

In this work we summarized some first results from our analysis of a few approaches to model the JWST PSF. Numerous PSF approaches exist, and we have given a basic description of the many tools that are being used within the JWST Project. We concentrated our efforts on using relatively simple optical modeling tools to assess which quantities can be reliably estimated without resorting to integrated modeling. We described and compared a number of quantities of interest to astronomical investigations, including the Encircled Energy, the Full Width at Half Maximum (FWHM), and the sharpness. We discussed the main PSF properties that will be common to all JWST science. We examined the differences between PSFs modeled using different error budget realizations, all fitting within the JWST error budget, and showed that even apparently small changes in the measured WFE can lead to large variations in the PSF morphology. We also calculated the expected dependence of the PSF on wavelength. While we expect JWST will exhibit a variable and potentially unpredictable PSF, we have also shown that the quality of that PSF will still exceed that currently observed by both HST and Spitzer for the wavelengths these missions have in common with JWST.

This report has been a first step towards providing JWST users a basic understanding of the PSF properties that they'll have to deal with, and a description of the modeling tools that may be of relevance to them. These same tools should also be of value to the JWST Science and Operations Center at STScI, since they can be used to assess the impact of various operational scenarios on PSF quality, and as a consequence, on the science output of the mission.

10.0 References

Anderson, J., & King, I.R., 2000, PASP, 112, 1360

Born, M., & Wolf, E. 1999, Principles of Optics (7th ed.; Cambridge: Cambridge Univ. Press)

Bracewell, R. 2000, The Fourier Transform and Its Applications (3rd ed.; New York: McGraw-Hill)

Bracewell, R. 2003, Fourier Analysis and Imaging (New York: Kulwer Academic / Plenum Publishers)

Bronowicki, A. et al. 2007, “SDR4 Analysis Cycle Summary Report,” 06-JWST-0593, (Boulder: BATC)

Casertano, S., 2002, "Some Considerations on PSF Asymmetry and its Impact on the Measurement of Galaxy Shapes," JWST-STScI-000396, (Baltimore: STScI)

Cox, C. & Hodge, P. 2006, in “Space Telescopes and Instrumentation I: Optical, Infrared, and Millimeter”, eds. J. C. Mather, H. A. MacEwen, & M. W. M. de Graauw, Proceedings of the SPIE, V. 6265, 62650W

Dean, B. and the JWST Wavefront Sensing and Control Team 2007, “TRL-6 for JWST Wavefront Sensing and Control”, (Greenbelt: GSFC)

Goodman, J. 2005, Introduction to Fourier optics, (3rd ed., Englewood, CO: Roberts & Co. Publishers)

Holfeltz, S.T., & Calzetti, D., 1999, "NIC 2 Growth Curves", Instrument Science Report NICMOS-99-007, (Baltimore: STScI)

Kaiser, N., Squires, G., & Broadhurst, T., 1995, ApJ, 449, 460

Makidon, R.B., Lallo, M.D., Casertano, S., Gilliland, R.L., Sirianni, M., & Krist, J.E., 2006, in "Observatory Operations: Strategies, Processes, and Systems", eds. D.R. Silva, and R.E. Doxsey, Proceedings of the SPIE, V. 6270, 62701L

Pavlovsky, C., et al., 2006, "Advanced Camera for Surveys Instrument Handbook for Cycle 16", Version 7.1, (Baltimore: STScI).

Sirianni, M., Jee, M.J., Beni'tez, N., Blakeslee, J.P., Martel, A.R., Meurer, G., Clampin, M., De Marchi, G., Ford, H.C., Gilliland, R., Hartig, G.F., Illingworth, G.D., Mack, J., & McCann, W.J. 2005, PASP, 117, 1049